Engineering Structures 177 (2018) 210–233

Contents lists available at ScienceDirect

Engineering Structures

journal homepage: www.elsevier.com/locate/engstruct

Comparative analysis of numerically simulated and experimentally measured motions and sectional forces and moments in a floating wind turbine hull structure subjected to combined wind and wave loads

Chenyu Luan*, Zhen Gao, Torgeir Moan

Norwegian Research Centre for Offshore Wind Technology (NOWITECH), NO-7491 Trondheim, Norway
Centre for Ships and Ocean Structures (CeSOS), NTNU, NO-7491 Trondheim, Norway
Centre for Autonomous Marine Operations and Systems (AMOS), NTNU, NO-7491 Trondheim, Norway
Department of Marine Technology, NTNU, NO-7491 Trondheim, Norway

ABSTRACT

Multi-body time-domain finite element models, which implement a recently developed numerical approach for determining forces and moments in floaters, are developed to simulate rigid-body motions and sectional forces and moments of a reference 5-MW braceless semi-submersible wind turbine in turbulent winds and irregular waves corresponding to below rated, at rated and above rated conditions. The simulated responses are compared with measurements of a 1:30 scaled model test using a real-time hybrid testing approach. In general, agreement between simulations and measurements are very good. Differences in spectral densities of the measurements and simulations have been quantified while the reasons for the differences have been thoroughly analyzed and discussed based on comparisons of measurements in different conditions and numerical parametrical study. Effects of non-linear wave excitation loads and drag forces on the rigid-body motions and sectional forces and moments are analyzed while dominant load components in fore-aft bending moments in five cross-sections in the hull of the reference model are identified. The interface between the pontoons and central column of the reference model is identified as the most critical part. Both low frequency and wave frequency load effect should be accounted for. Mean forces and moments from wind and waves result in a change in configuration of mean wetted body surface of the hull when compared to its configuration in calm water. This may result in a considerable change in resultant sectional forces and moments even though change in resultant of the hydro pressure forces on whole of the wetted body surface could be very limited. For the analyzed model, simulated fore-aft bending moments of the model in wind and waves could be obtained by superimposing the results for wind only condition, and wave only condition except that the corresponding averaged wind induced forces and moments should be applied on the numerical model. This simplification can significantly reduce number of cases of short-term analysis required in long-term analysis. However, applicability of the simplification should be analyzed case by case in particular for a blunt structure with relatively large volume of displaced water in waves with relatively small wave length. Analysis and discussions given in this paper are based on available measurements of the model test. Hydroelastisity and structural vibration of the columns and pontoons of the hull are not accounted for by the numerical and experimental models. Suggestions for design of future model tests are given in this paper.

1. Introduction

Floating wind turbines are considered an attractive solution for harvesting offshore wind energy in relatively deep water, e.g. deeper than 80 m. In general, a floating wind turbine is composed of a Rotor Nacelle Assembly (RNA), a tower, a hull and a mooring system.

As required by relevant standards and guidelines for offshore wind turbines, e.g. [1–5], global responses, in terms of motions and sectional forces and moments, should be appropriately analyzed for limit state design checks. As the development of floating wind turbines is at an early stage, numerical simulations and model tests for analyzing the global responses of floating wind turbines in wind and waves are hot research topics.

Computer codes for analyzing floating wind turbines have been developed by combining the knowledge and computer codes for modelling hydro loads on offshore platforms and aerodynamic loads on land-based wind turbines for decades [6]. A review of conventional approaches for modelling aerodynamic loads on the RNA and tower, hydro loads on the hull and mooring lines of floating wind turbines is available in [7]. Features of some conventional time-domain computer codes are tabulated in [8]. Global responses of the RNA, tower, and mooring system, and rigid-body motions of a given floating wind turbine can be simulated in these codes by generating and solving finite element model for the floating wind turbine, while Morison formula and/or the conventional hybrid frequency-time domain approach [9] is used to model hydro loads on the hull of the floating wind turbine. Morison formula is an empirical formula and, in general, applicable when wave length is larger than five times the diameter of the slender

* Corresponding author at: Department of Marine Technology, Norwegian University of Science and Technology (NTNU), NO-7491 Trondheim, Norway.
E-mail addresses: chenyu.luan@ntnu.no (C. Luan), zhen.gao@ntnu.no (Z. Gao), torgeir.moan@ntnu.no (T. Moan).

https://doi.org/10.1016/j.engstruct.2018.08.021
Received 26 November 2017; Received in revised form 9 August 2018; Accepted 10 August 2018
Available online 01 October 2018
0141-0296/ © 2018 The Authors. Published by Elsevier Ltd. This is an open access article under the CC BY-NC-ND license (http://creativecommons.org/licenses/BY-NC-ND/4.0/).

structure's cross-section [10]. The computer codes which implement the conventional hybrid frequency-time domain approach cannot capture the sectional forces and moments in the hull since the hull is modelled as a rigid-body with 6 d.o.f.s in the finite element model. Luan et al. [9] recently developed an approach based on an extension of the conventional hybrid frequency-time domain approach, for which the hull is modelled as multi-bodies. The developed approach can be easily implemented in various state-of-the-art time-domain computer codes for floating wind turbines, e.g. Simo/Riflex/Aerodyn, OrcaFlex and FAST + CHARM3D, to extend their capabilities to analyze sectional forces and moments in structural components of a generic floater. A moderate wave-only experimental validation for this approach is made in [11].

Global responses of floating wind turbines in wind and waves can be measured (and analyzed) by carrying out model tests. Conventional model tests for measuring wave induced responses of a floating unit are designed to satisfy geometrical and kinematic similarities and equality according to Froude number ensure similarity between inertia and gravity forces of the experimental and actual models. However, similarity between inertia and viscous forces of the models cannot be achieved since, in practice, equality in Reynolds number cannot be satisfied at the same time. Different Reynolds number may indicate different patterns of fluid flows around the experimental and actual models. Necessary corrections are needed if the measurements are sensitive to the viscous forces. Due to the same reason, similarity between inertia and aerodynamic loads on the RNA, which are important to responses of floating wind turbines, cannot be achieved either, see [12–14]. To solve this problem, various forms of "non-geometrical scaling" of the wind turbine rotor have been developed to improve the aerodynamic load modeling in wind-wave model tests. For example, one form of non-geometrical scaling is to replace the wind turbine rotor with a drag disk, e.g. [15,16]. A more sophisticated method of non-geometrical scaling is to modify the wind turbine airfoil shape and chord length to obtain improved performance at low Reynolds numbers [17–20]. These non-geometrical scaled wind turbines can be designed to achieve the same non-dimensional thrust coefficient as the reference full scale wind turbine in a specified steady condition (calm water, constant wind speed, and fixed rotational speed and pitch angle of the blades). Therefore, the "non-geometrical scaled" wind turbines can be used to physically analyze static response of the experimental model of floating wind turbines in steady conditions. However, it is still a challenge, which has not been solved yet, to make a performance-matched wind turbine model, which means to use the non-geometrical scaled wind turbines in model tests to accurately mimic Froude scaled actual aerodynamic loads on the rotor of the corresponding full scale reference wind turbine in dynamic conditions (turbulent winds, and/or regular or irregular waves, and/or with or without controller for blade pitch angle and rotational speed). This is because it is a challenge to design a non-geometrical scaled wind turbine for which the non-dimensional thrust coefficient is always identical to the corresponding coefficient of the reference full scale wind turbine in an arbitrary steady condition. As shown in [17], the non-dimensional thrust coefficient versus tip speed ratio curves of the non-geometrical scaled wind turbines can be very sensitive to the wind speed (the Reynolds number). It is also a challenge to generate and/or measure constant and turbulent wind fields in a classical towing tank or ocean basin [21] as well. Implementation of real-time hybrid model testing approach, e.g. ReaTHM® [22], and reference [23], is a recent development for accurate modelling the actual aerodynamic loads in ocean basin. ReaTHM® relies on the assumption that actual aerodynamic loads on the full scaled reference wind turbine can be captured by the state-of-the-art aerodynamic computer codes, e.g. Aerodyn [24]. A numerical finite element model for the RNA and control system of the full scale reference wind turbine and numerical model of wind field are generated in a computer code which implements the state-of-the-art aerodynamic computer code to calculate the aerodynamic loads on the RNA in the wind field. The resultants of the calculated aerodynamic loads are down scaled (based on Froude scale) and physically applied on a Froude scaled model of the floating wind turbine, while in the computer code the hub of the RNA rigidly follows the measured rigid-body motions, which has been up scaled (based on Froude scale), of the experimental model. A 1:30 scaled braceless semi-submersible model test which implements the ReaTHM® testing approach was done by SINTEF Ocean in its ocean basin [25]. Sectional forces and moments in base of a side column and tower base of the model in different combined wind and wave conditions have been measured. ReaTHM® can appropriately address effects of the control system on the aerodynamic loads while the actual loaded forces can be measured in a straight-forward manner. A detailed description of the approach and its feasibility is available in [22,26].

This paper intends to shed more light on sectional forces and moments in the hull of semi-submersible wind turbines submitted to combined wind and wave loads by thoroughly analyzing the measurements of the 1:30 scaled model test in SINTEF Ocean and corresponding numerical simulations. A Simo/Riflex model which implements the approach presented by Luan et al. [9] has been generated. Sectional forces and moments in five cross-sections of the hull of the braceless semi-submersible wind turbine are analyzed. The hull of the braceless semi-submersible wind turbine is a static determinate structure. The external load on the hull is composed of wave excitation loads, added mass forces, potential damping forces, gravity, hydrostatic forces, and drag forces. Configurations of mean wetted body surface of the model in wind and waves and in wave only are different due to mean components of the wind loads on the rotor, tower and hull of the model. The difference means that hydrodynamic coefficients that are calculated for modeling hydro loads on the hull are different since values and distributions of hydro pressure forces on the hull are changed. Numerical sensitivity study and comparisons of measurements in different conditions are used to analyze effects of each component of the external loads, and inertial load on the sectional bending moments in different cross-sections of the hull. Simplifications for the numerical modelling are discussed based on the results of the parametric analysis. Sectional forces and moments in different cross-sections are compared. To quantify the differences between the numerical model and the experimental model, the simulated and measured fore-aft bending moments in the bases of the side column and tower are compared. The agreement is reasonably good.

In previously, comparisons of simulated and measured responses of floating wind turbines have been analyzed by some researchers, e.g. [27]. Geometrical scaled or non-geometrical scaled wind turbine, which cannot correctly mimic the Froude scaled aerodynamic loads on the corresponding full scale reference wind turbine in dynamic condition, are used in the model tests mentioned by the researchers in their publications, while these model tests are not designed for capturing sectional forces and moments in hull of floating wind turbines. For each model test, the wind turbine of the experimental model is modelled in its corresponding numerical model to simulate aerodynamic loads on the wind turbine while numerical wind field is generated based on measured wind speed at one specified fixed position in the model test. Consequently, the differences between the measurements and simulations are due to the differences between 1) the numerical wind field and actual wind field in the model test, 2) performance of the numerical and experimental models of the wind turbine and 3) mass properties of the numerical and experimental models and 4) hydro loads on the hull of the numerical and experimental models. These differences are mixed and make it difficult to analyze reasons for the differences between the measurements and simulations in quantity. To avoid this difficult situation, the aerodynamic loads which are actually loaded on the 1:30 scaled model analyzed in this paper are measured and loaded on their corresponding numerical model to ensure identical aerodynamic loads. As analyzed in detail later in this paper, although the aerodynamic loads are loaded as prescriptive loads the differences between the measurements and simulations only indicate differences in the hydro

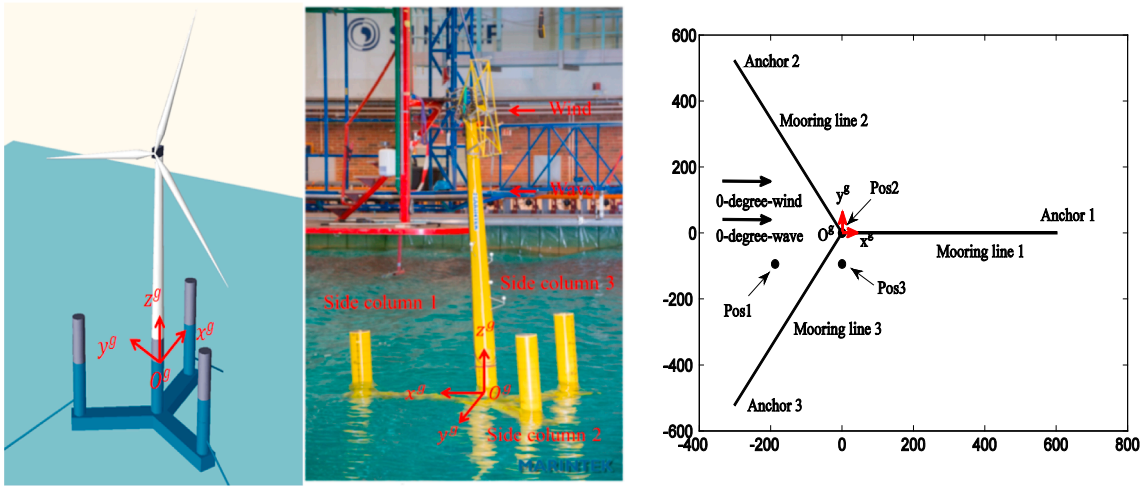

Fig. 1. Layout of the experimental model.

loads on the hull and the mass properties of the numerical and experimental models. The differences in the mass properties can be reduced to a negligible level by carrying out quality control and calibrations. The differences in each component of the hydro loads are analyzed in this paper.

2. Model tests

A layout of the experimental model, the Earth-fixed coordinate system (O^g-x^g-y^g-z^g) and load directions are shown in Fig. 1. O^g is at geometrical center of water plane area when the model is in calm water. The specified dimensions of the semi-submersible hull are tabulated in Table 1 and shown in Fig. 2. The mooring system is composed of three catenary chain mooring lines. Each mooring line has two segments from fairlead to anchor with constant solid circular cross-section. Design parameters are given in Tables 2 and 3. The scaled value of the Young's modulus of the mooring lines of the experimental model is $6.3*10^9$ kN/m^2. Measured mass properties of the hull are given in [25]. However, as analyzed in [11], calibrated rather than measured mass properties are eventually used in development of numerical models due to the "model-the-model" principle which means to simulate the actual model tests as closely as possible [28]. The calibrated mass properties are given in Section 3, describing the numerical models used in this paper. Note that all the data and results presented and discussed in this paper are given in full scale and in the corresponding coordinate systems described in this paper. A linear scaling factor of $\lambda = 30$ and the Froude scaling law are used to scale the original data measured from the model test. Environmental conditions of the model tests are tabulated in Table 4. Fore-aft bending moments in the base of the side column 1 and tower are measured. A more detailed description of the model tests is found in [11,25].

Table 1
Specified dimensions of the semi-submersible hull (Full-scale).

Central column diameter [m]	6.5
Side column diameter [m]	6.5
Pontoon height [m]	6
Pontoon width [m]	9
Central column freeboard [m]	10
Side column freeboard [m]	20
Center-to-center (central to side column) [m]	41
Center-to-edge (central column to pontoon end) [m]	45.5
Operating draft [m]	30
Displacement [tonne]	10,555

3. Numerical models and calibrations

3.1. Numerical models

Simo and Riflex [29,30] are used to simulate sectional forces and moments in five cross-sections (denoted as SX, X = 1, 2,…,5) in the hull of the semi-submersible wind turbine. S1 represents a horizontal cross-section on the base of side column 1. S2 and S3 are vertical cross-sections on Pontoon 1. S4 is a horizontal cross-section on base of central column. S5 is a horizontal cross-section on the base of tower, see Fig. 2. The geometrical center of the cross-sections are tabulated in Table 5 in a body-fixed coordinate system (denoted as O^b-x^b-y^b-z^b) which coincides with the global coordinate system (O^g-x^g-y^g-z^g) when the wind turbine is located in calm water. Each cross-section divides the model into two part: Part A and B. We denote the part which includes the tower and RNA as Part B, see Fig. 2 for an example.

Key features and limitations of the developed numerical models are highlight as follows:

- A time-domain finite element model is generated to simulate sectional forces and moments.
- Effect of flexible modes of the hull and tower on motions and sectional forces and moments (effect of hydroelasticity) is negligible as the hull and tower of the experimental model is stiff.
- Wave excitation and radiation loads on Parts A and B are modelled by using hydrodynamic coefficients that are obtained by solving a first order boundary value problem based on corresponding mean wetted body surface of the hull with rigid-body assumption for the hull. The second and higher order wave loads on the hull are not modelled except for the drag forces which are modelled by the drag term of Morison formula.
- The measured aerodynamic loads are applied on Part B as prescriptive loads. The differences between the measurements and simulations only indicate the differences in the hydro loads on the hull and the mass properties of the numerical and experimental models.
- Necessary calibrations are carried out to reduce uncertainties between the numerical and experimental models.
- Luan et al.'s approach is available to a generic floater (with a static determinate or indeterminate structure). The numerical models used in this paper are its specific applications. More detailed descriptions and limitations of the approach are referred to [9].

A detailed description of the developed numerical models is given as follows:

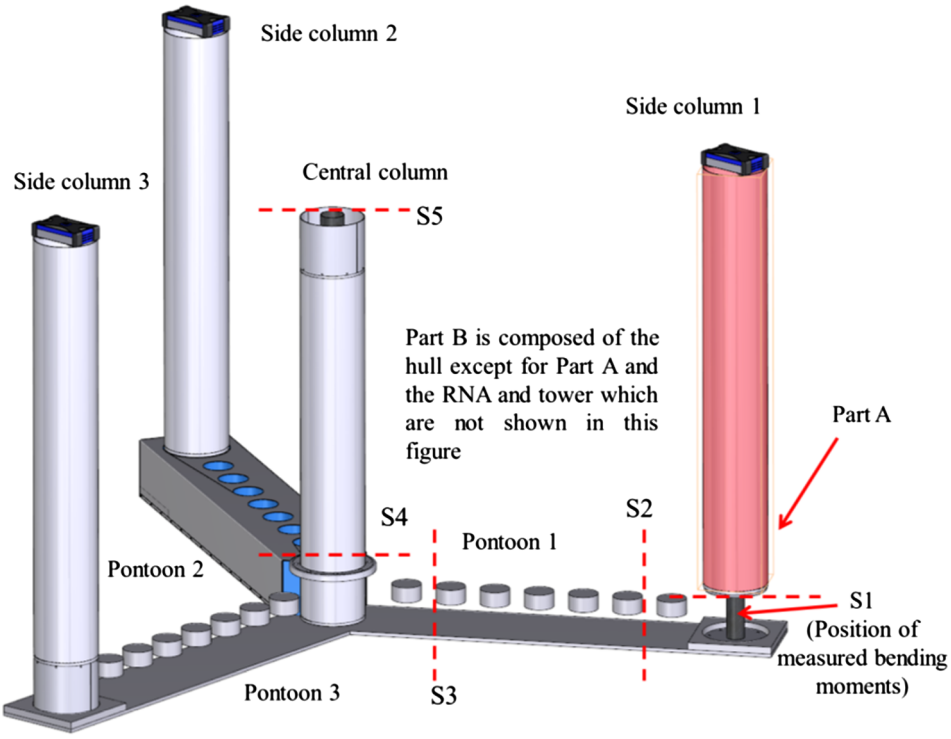

Fig. 2. A layout of the hull of the experimental model, courtesy of Fredrik Brun (SINTEF Ocean). Note that the configurations of the three pontoons are identical. Some parts of the configurations of Pontoon 1 and 3 are not shown.

Table 2
Design parameters of a single mooring line (Full-scale).

Segment	Length (m)	Mass per length (kg/m)	Wet weight (kN/m)	Specified diameter (m)
Upper	240.00	235.0	2.005	0.195
Lower	367.55	446.0	3.804	0.269

Table 3
Arrangement of the mooring line anchors and fairleads described in the global coordinate system (Full-scale).

Fairlead	x^g	y^g	z^g	Anchor	x^g	y^g	z^g
1	45.95	0	−27	1	603	0	−200
2	–22.98	39.8	−27	2	−301.5	522.2	−200
3	–22.98	−39.8	−27	3	−301.5	−522.2	−200

To simulate sectional forces and moments in a given cross-section, a time-domain finite element model is generated and solved in Riflex in the global coordinate system. The model is composed of 183 truss elements for modelling the three mooring lines, three artificial beam elements for capturing sectional forces and moments in the corresponding cross-section and two control nodes for modelling external and inertial loads on the corresponding Parts A and B.

Table 5
Positions of geometrical center of the five cross-sections in the body fixed coordinate system.

	S1	S2	S3	S4	S5
x^b_{SX}	41	31.5	7.5	0	0
y^b_{SX}	0	0	0	0	0
z^b_{SX}	−27	−27	−27	–22	10

If we denote location of geometrical center of SX as $(x^b_{SX}, y^b_{SX}, z^b_{SX})$ in the O^b-x^b-y^b-z^b coordinate system, positions of end nodes of the corresponding artificial beams are given in Table 6. The artificial beam elements are massless. There are no external loads on the artificial beam elements. Each artificial beam element only has axial and torsional stiffness. The columns and pontoons of the experimental model are designed to have sufficient stiffness to make hydroelasticity effects on the model negligible. Therefore, for each artificial beam element, the product of the Young's modulus and cross-section area is specified as

Table 4
Environmental conditions of selected model tests (Full-scale).

Reference no.	H_s [m]	T_p [s]	Mean wind speed at nacelle [m/s]	Turbulence intensity factor [%]	Direction of waves [degree]	Direction of winds [degree]	Model test duration [h]	Note
2410	15.3	14	None	None	0	None	3	Irregular wave only condition. JONSWAP
2420	3.6	10.2	None	None	0	None	3	wave spectrum
1713	None	None	11	17.0	None	0	3	Turbulent wind only condition. Kaimal
1733	None	None	25	13.2	None	0	3	wind spectrum
4121	5.9	11.3	25	13.2	0	0	3	Turbulent wind and irregular waves.
4132	5.9	11.3	25	13.2	0	0	3	JONSWAP wave spectrum and Kaimal
4310	3.6	10.2	11	17.0	0	0	3	wind spectrum. In operation
4410	5.2	8	8	19.5	0	0	3	

Table 6
Positions of end nodes of the three artificial beams that correspond to the SX in the body-fixed coordinate system (Units in meter).

	End 1	End 2
Artificial beam 1	(x^b_{SX} -0.1, y^b_{SX}, z^b_{SX})	(x^b_{SX} +0.1, y^b_{SX}, z^b_{SX})
Artificial beam 2	(x^b_{SX}, y^b_{SX} -0.1, z^b_{SX})	(x^b_{SX}, y^b_{SX} +0.1, z^b_{SX})
Artificial beam 3	(x^b_{SX}, y^b_{SX}, z^b_{SX} -0.1)	(x^b_{SX}, y^b_{SX}, z^b_{SX} +0.1)

10^9 kN, while, the product of the torsional rigidity and modulus of rigidity are specified as 10^9 kN m^2/rad.

The external and inertial loads on Parts A and B are modelled in Simo by using the Luan et al's approach which is initially described in [9] and applied on the control nodes in the finite element model generated in Riflex. Each control node has 6 d.o.f.s. Each of the end nodes of the artificial beam elements and the top end nodes of the mooring lines (the fairleads) rigidly follows the motions of the corresponding control node.

We denote position of the control nodes corresponding to the corresponding Parts A and B for the cross-section SX in the global coordinate system as $\boldsymbol{\eta}^{SX,A}(t)$ and $\boldsymbol{\eta}^{SX,B}(t)$, respectively. $\boldsymbol{\eta}^{SX,A}(t)$ and $\boldsymbol{\eta}^{SX,B}(t)$ are 6×1 vectors and used to represent motions of the Parts A and B. When the floating wind turbine is in calm water, the control nodes are located at the origin of the global coordinate system while all of the terms in $\boldsymbol{\eta}^{SX,A}$ and $\boldsymbol{\eta}^{SX,B}$ are zero.

Body related coordinate systems for Parts A and B corresponding to cross-section SX are generated in Simo and denoted as $O^{r,A,SX}$-$x^{r,A,SX}$-$y^{r,A,SX}$-$z^{r,A,SX}$ and $O^{r,B,SX}$-$x^{r,B,SX}$-$y^{r,B,SX}$-$z^{r,B,SX}$, respectively. The O^b-x^b-y^b-z^b and body-related coordinate systems are coincident when the model is located at its mean position in calm water. $O^{r,A,SX}$ and $O^{r,B,SX}$ rigidly follow rigid-body motions of the O^b but the orientation of the body-related coordinate systems and the vertical position of the $O^{r,A,SX}$ and $O^{r,B,SX}$ are fixed (as the same as the body-related coordinate systems when the model is located at its initial position in time-domain simulation).

Applying Luan et al.'s approach, the first order wave excitation and radiation loads are modeled as forces and moments acting on the $O^{r,A,SX}$ and $O^{r,B,SX}$, while the forces and moments are determined by corresponding hydrodynamic coefficients and first and second derivative of $\boldsymbol{\eta}^{SX,A}(t)$ and $\boldsymbol{\eta}^{SX,B}(t)$ and wave elevation of incident waves.

The hydrodynamic coefficients are obtained by the following steps, 1) generating and solving a boundary value problem based on corresponding mean wetted body surface in O^f-x^f-y^f-z^f coordinate system (an earth fixed coordinate system) with rigid-body assumption for the hull, 2) calculating pressure forces on the mean wetted body surface based on the Bernoulli's equation and corresponding velocity potential, 3) integrating the pressure on the wetted body surface of the corresponding Part A or B using the coordinate system O^f-x^f-y^f-z^f to obtain the integrated forces and moments acting on the O^f, and 4) derive the hydrodynamic coefficients based on the corresponding resultant forces and moments on the O^f in the O^f-x^f-y^f-z^f coordinate system.

Wind and wave loads on floating wind turbines have a steady (constant) component. The component is composed of constant forces and moments and results in a mean horizontal offset and title angle. Phase angle of each frequency component of incident wave should be updated based on the mean horizontal offset in particular for high frequency components which can be very sensitive to the mean horizontal offset. The configuration of the mean wetted body surface in the O^f-x^f-y^f-z^f coordinate system should be updated based on the mean title angle. The mean wetted body surfaces of the hull corresponding to 0-degree and α-degree tilt angles in the O^f-x^f-y^f-z^f coordinate system are shown in Fig. 3.

Morison's formula is used to model the hydrodynamic loads on the mooring lines, while the drag term of the Morison's formula is use to model the drag forces on the hull components. Non-dimensional drag and mass coefficients (C_d and C_a) for the segments of each mooring line are specified as 1.4 and 1.0 respectively, while C_d for width and height of the pontoons and columns are specified as 2.1, 1.7 and 0.5, respectively, according to [31]. Young's modulus of mooring lines of the numerical model is specified as $2.1*10^8$ kN/m^2 rather than $6.3*10^9$ kN/m^2, which is obtained by upscaling the measured value of the experimental model, to avoid numerical problems. In theory, the effect of this difference on mooring line tension and global responses of the model are negligible.

Aerodynamic loads which were applied on the experimental model were measured. The measured aerodynamic loads are applied on the control node for Part B to model the aerodynamic loads.

The numerical models do not include the second order and higher order hydrodynamic loads and hydroelastical effects except for the viscous drag forces, while the numerical models include hydrodynamic interactions between Parts A and B.

In Riflex, the time-domain finite element model is solved by using Newmark-β numerical integration ($\beta = 3.9$ and $\gamma = 0.505$). Time step is set to be 0.05 s. Rayleigh damping, which is a linear combination of the Riflex generated global mass and stiffness matrices, is used for modelling effect of structural damping. The corresponding mass and stiffness proportional coefficients are set to be 0 and 0.005, respectively. More explanations are given in [30].

3.2. Calibrations

The "model-the-model" principle, which means to simulate the actual model tests as closely as possible [18], is used. As discussed in [11,32], the anchors of the mooring lines are moved 1.5 meters away along the radial direction. The mass of the experimental model can be estimated based on the draft, configuration of the hull and resultant force of the vertical components of the mooring line tensions at the fairleads. Comparing the estimated mass to the measured mass, a 4.7% deviation is observed (Note that the difference due to the weight of the mooring lines has already been considered). Meanwhile there are discrepancies between the simulated and measured roll/pitch natural periods (obtained from decay tests) and mean heeling angle and fore-aft and side-to-side bending moment in turbulent wind-only conditions. As discussed in [32], deviations may exist in the measurements of the position of the center of gravity and moment of inertia. Consequently, a constant force is added to compensate the 4.7% difference and make the numerical model float at the same draft as the experimental model in calm water while the vertical position of the center of gravity and mass matrix of the corresponding Parts A and B are calibrated. Mass properties used in the numerical models are tabulated in Table 7. The procedure for calibrating the mass properties of the whole model and Parts A and B corresponding to S1 has been presented in [11]. Note that three forces and moments were used to adjust the inertial loads of Part B (corresponding for S1) and denoted as $-\boldsymbol{M}^{addi}_{mass}\ddot{\boldsymbol{\eta}}^{S1,B}(t)$. The $\boldsymbol{M}^{addi}_{mass}$ is a 6×6 matrix. The $\ddot{\boldsymbol{\eta}}^{S1,B}(t)$ is the second derivative of the $\boldsymbol{\eta}^{S1,B}(t)$. The three forces and moments are described in the $O^{r,B,S1}$-$x^{r,B,S1}$-$y^{r,B,S1}$-$z^{r,B,S1}$ coordinate system with respect to the $O^{r,B,S1}$. According to the results of a parametric study with respect to the effect of each term in the $\boldsymbol{M}^{addi}_{mass}$ on the motion responses and bending moments, all the terms in the $\boldsymbol{M}^{addi}_{mass}$ are zero except for $M^{addi}_{mass,11} = M^{addi}_{mass,22} = 571$ tonnes and $M^{addi}_{mass,24} = M^{addi}_{mass,42} = 5690$ tonnes $*$ m^2. Relative differences between the adjusted terms and the corresponding terms in the original measured mass matrix of Part B are less than 6%. As shown in [11], agreement between measured and simulated rigid-body motions and fore-aft bending moments in cross-section S1 of the semi-submersible wind turbine in moderate wave-only conditions is very good. Therefore, the same calibrated mass properties are used in the present paper while the same procedure is used to calibrate mass properties of Parts A and B corresponding to S5. We do not have any measurements to calibrate mass properties of Parts A and B corresponding to cross-section S2, S3 and S4. Therefore, these mass properties are reasonably estimated by

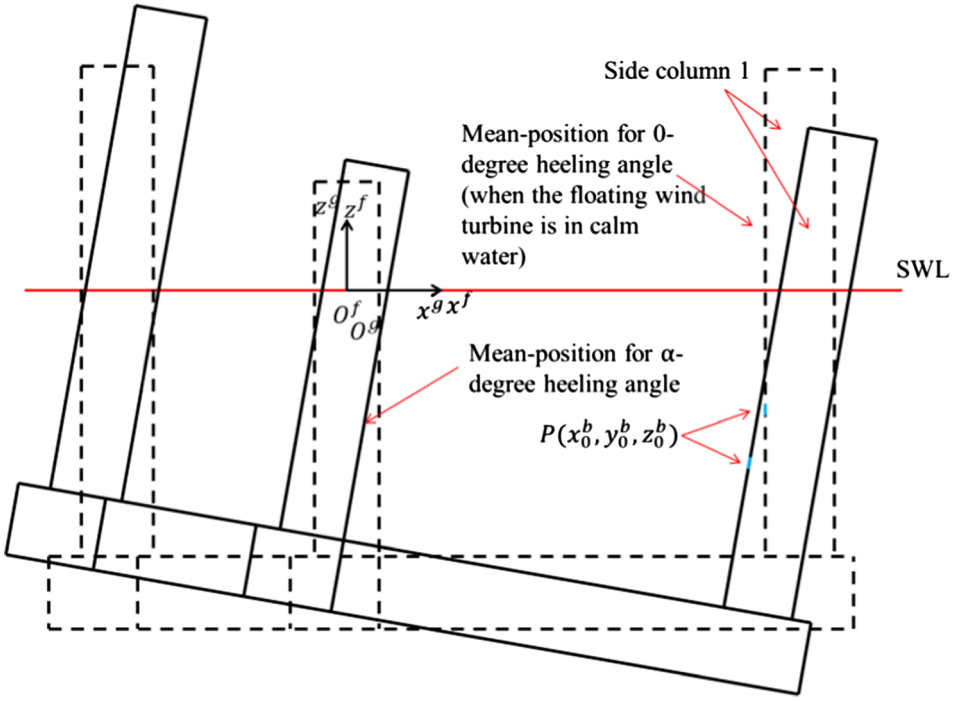

Fig. 3. Configuration of mean wetted body surface of the hull subjected to different title angles.

the authors according to the calibrated mass properties and mass distribution of the original design described in [33].

In numerical models for simulating sectional forces and moments in S1, S2 and S3, an inertial load vector ($-\boldsymbol{M}_{mass}^{addi}\ddot{\boldsymbol{\eta}}^{SX,B}$), a quadratic damping force vector ($-\boldsymbol{D}_{Q}^{addi}|\dot{\boldsymbol{\eta}}|^{SX,B}\dot{\boldsymbol{\eta}}^{SX,B}$) and a restoring load vector ($-\boldsymbol{K}_{rest}^{addi}\boldsymbol{\eta}^{SX,B}$), $\boldsymbol{X}$ = 1, 2, or 3, are added on the control node corresponding to the corresponding Part B. Forces and moments presented by the vectors are described in the $O^{r,B,SX}$-$x^{r,B,SX}$-$y^{r,B,SX}$-$z^{r,B,SX}$ coordinate system with respect to the $O^{r,B,SX}$, $\boldsymbol{X}$ = 1, 2, or 3. $\boldsymbol{D}_{Q}^{addi}$ and $\boldsymbol{K}_{rest}^{addi}$ are 6×6 matrixs. All terms in $\boldsymbol{K}_{rest}^{addi}$ are zero except for $K_{rest,11}^{addi} = -8$kN/m and $K_{rest,15}^{addi} = K_{rest,51}^{addi} = -80$kN m/m. All terms in $\boldsymbol{D}_{Q}^{addi}$ are zero except for $D_{Q,55}^{addi} = 40,013,494$kN m s^2/rad^2 for model tests 4410 and 4310. Note that the quadratic damping force vector is not added on the numerical models for test 4121. Similarly, $-\boldsymbol{M}_{mass}^{addi}\ddot{\boldsymbol{\eta}}^{SX,A}$, $-\boldsymbol{D}_{Q}^{addi}|\dot{\boldsymbol{\eta}}|^{SX,A}\dot{\boldsymbol{\eta}}^{SX,A}$ and $-\boldsymbol{K}_{rest}^{addi}\boldsymbol{\eta}^{SX,A}$, $\boldsymbol{X}$ = 4 or 5, is added on the control node corresponding to the corresponding Part A in the numerical models corresponding for S4 and S5.

These added forces and moments, to some extent, affect rigid-body motions of the model, in particular for low frequency components of the motions. Consequently, components of sectional forces and moments in the cross-sections that are related to motions, velocities and accelerations are affected by these added forces and moments. While, comparing to forces and moments in the specified cross-sections, the added forces and moments are negligible.

4. Comparisons for measured and simulated responses in operational conditions

Simulated and measured rigid-body motions and fore-aft sectional bending moments of the model in combined wind and wave conditions, i.e. model test 4410, model test 4310 and model test 4121, are compared.

The differences between the measurements and simulations are related to uncertainties in the measurements and the differences between the actual and simulated inertial and external loads on the semi-submersible wind turbine. In another word, the simulated and measured responses, e.g. rigid-body motions and sectional forces and moments, will be identical, if the simulated and actual inertial and external loads are identical, and the actual responses can be accurately measured. The external loads are composed of aerodynamic loads, hydro loads and gravity forces. We can assume that the differences between the simulated and actual aerodynamic loads are negligible since the measured aerodynamic loads are applied on the numerical model as prescriptive loads. While, as analyzed by [25,26], we can assume that sensors used in the model test can accurately measure the rigid-body motions, fore-aft sectional bending moments, wave elevation and the actual applied aerodynamic loads on the experimental model.

Consequently, differences in simulated and measured responses indicate differences between simulated and actual inertial loads, gravity

Table 7
Mass properties of the numerical models. The center of gravity is described in the body-fixed coordinate system with respect to O^b. The moments of inertia are about the center of gravity.

	Mass [tonnes]	Centre of gravity [m]			Moments of inertia [tonnes*m^2]					
		x^b	y^b	z^b	I_{xx}	I_{yy}	I_{zz}	I_{xy}	I_{xz}	I_{yz}
Complete model	9730.0	0	0	−20.35	10,308,320	10,293,841	7,637,715	0	20,759	0
Part A for S1	456.7	41	0	−12.93	96,093	96,093	2193	0	0	0
Part A for S2	1422.7	37.6	0.0	−24.6	170,571	193,411	27,594	0.0	0.0	−25,754
Part A for S3	2574.7	29.5	0.0	−26.7	187,382	474,115	295,068	0.0	0.0	−79,897
Part A for S4	8712.0	0.0	0.0	−27.9	4009202.0	4080202.0	7638356.0	0.0	0.0	19947.0
Part A for S5	8873.2	0.0	0.0	−27.5	4105877.0	4173877.0	7640000.0	0.0	0.0	19947.0

forces and hydro loads.

The differences between simulated and actual inertial loads and gravity forces are related to uncertainties in the mass properties and the differences in measured and simulated rigid-body motions. As analyzed in [11,32] and Section 3.2 of this paper, measurements of the mass properties and configurations of the mooring lines and hull of the experimental model may be uncertain. Therefore, essential calibrations are carried out to reduce these uncertainties, see Section 3.2.

Objective of this section is to identify differences between the simulated and actual hydro loads via comparing the simulated and measured responses.

Note that the developed numerical models cannot completely account for all the components of the second and higher order hydro loads however these loads inherently exist in the experimental tests. In addition, the drag term of Morison formula [31] is used to model the viscous drag forces on the hull and mooring lines. This is an empirical formula. While, the coefficients for simulating the viscous drag forces are determined according to the Reynolds number, Keulegan-Carpenter numbers and surface roughness which correspond to the full size model rather than the Froude law scaled model. Consequently, the drag coefficients need to be appropriately calibrated, see Section 3.2. The hydro loads can be further classified as wave excitation loads, radiation loads, and hydrostatic pressure forces, see [9]. Note that these loads are related to the configuration of the wetted body surface of the hull. The sensitivity study and comparisons of measurements in different conditions are used to analyze effects of these components on rigid-body motions and sectional bending moments, see Section 5. The effect of these components is used to identify reasons for the differences between the measurements and simulations presented in this section.

In this section, the measurements correspond to three different turbulent wind conditions, which includes turbulent winds with mean wind speed below (8 m/s), at (11 m/s) and above (25 m/s) the rated wind speed of the 5-MW wind turbine. 3-h realizations of wave elevation are generated in the time-domain models according to the corresponding 3-h realizations of the measured wave elevations; while the measured aerodynamic loads are loaded on the time-domain models, correspondingly. 1-h realizations of rigid-body motions and bending moments are selected from the 3-h simulated realizations by neglecting transient processes (first 1000 s of each realization).

Spectral density functions are obtained by applying inverse Fourier transform, with a fixed smoothing parameter, of the autocorrelation function of the 1-h realizations. Regarding the spectral density functions, we focus on spectral densities in frequency range of 0 rad/s to 2 rad/s. Major parts of areas under spectral density curves of incident wave-elevations and thrust forces and moments applied on the rotor are in wave-frequency-range (defined as from 0.3 rad/s to 2 rad/s) and low frequency-range (defined as from 0 rad/s to 0.3 rad/s), respectively, see Fig. 4. The turbine is in operational condition in these model tests.

Relative difference (n_r) of standard deviations of simulations and measurements are calculated based on the area under the corresponding spectral density curves in the corresponding specified frequency range, see Eq. (1) and [34]. In Eq. (1), $m_{0,s}$ represents the area of the part under the spectral density curve of a simulated response in a specified frequency range, i.e. full frequency-range, low frequency-range and wave-frequency-range. Similarly, $m_{0,m}$ represents the area of the part under the spectral density curve of a measured response in a specified frequency range.

$$n_r = \frac{\sqrt{m_{0,s}} - \sqrt{m_{0,m}}}{\sqrt{m_{0,m}}} * 100\% \tag{1}$$

We denote a simulated and a measured response as x and y, respectively. Transfer function between x and y can be calculated by using Eq. (2). G_{xy} and G_{xx} are one-side spectra that are derived from corresponding cross-correlation and autocorrelation with respect to the realizations of x and y, respectively [35]. $H_{xy}(\omega)$ is a complex number.

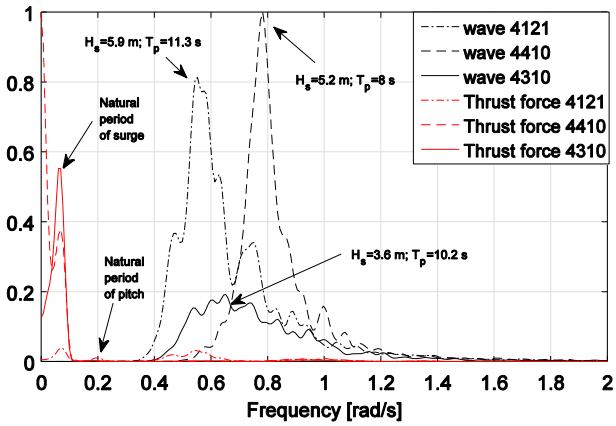

Fig. 4. Normalized spectral densities of wave elevations and thrust forces applied on the rotor.

Real and imaginary parts are denoted as *Re* and *Im* respectively. Phase angle (α) between x and y is derived based on the corresponding values of *Re* and *Im*.

$$H_{xy}(\omega) = \frac{G_{xy}(\omega)}{G_{xx}(\omega)} = Re + Im*i \tag{2}$$

4.1. Comparisons of measured and simulated rigid-body motions in operational conditions

In general, agreement between simulated and measured rigid-body motions, in terms of spectral densities and phase angle, is very good. Relative difference of standard deviations of simulated and measured pitch in full frequency-range is less than 4%. Differences in phase angle between simulated and measured motions are no more than 20 degrees, see Fig. 8. For the phase angles, we focus on the differences in frequency range from 0 rad/s to 1 rad/s since the responses in the rest frequency range are very limited.

Wave-frequency components in the surge and pitch motions are limited when compared to the corresponding low frequency components, see Figs. 5 and 6. As analyzed later in this paper, the difference between simulated and measured wave-frequency components in the surge and pitch motions could be induced by the second and higher order wave excitation loads which are inherently exist in the model tests but are not modelled in the numerical models and/or differences between the simulated and actual first order wave excitation loads on the hull. The agreement between wave-frequency components of the heave motion of the numerical and experimental models is very good (see Fig. 7).

Low frequency responses of the model with frequency components around its natural frequencies (0.073 rad/s for surge, 0.21 rad/s for pitch and 0.246 rad/s for heave) are sensitive to the second and higher order hydro loads (potential loads and viscous drags) and restoring stiffness, while low frequency responses of the model with frequency components less than 0.05 rad/s are sensitive to the restoring stiffness. As analyzed later in this paper, the differences between the measured and simulated heave motions with frequency components from 0.2 rad/s to 0.3 rad/s, and the surge motions with frequency components from 0 rad/s to 0.1 rad/s are due to differences in the second and higher order hydro loads of the numerical and experimental models. When the effect of the second and higher order hydro loads on the low frequency surge and pitch motions are relatively small (i.e. low frequency surge motion of model test 4310, and pitch motions of model test 4310, 4410 and 4121), very good agreement between simulated and measured surge and pitch motions can be achieved by adjusting (calibrating) restoring stiffness of the numerical mooring lines and quadratic damping coefficients. n_r for standard deviations of the simulated and

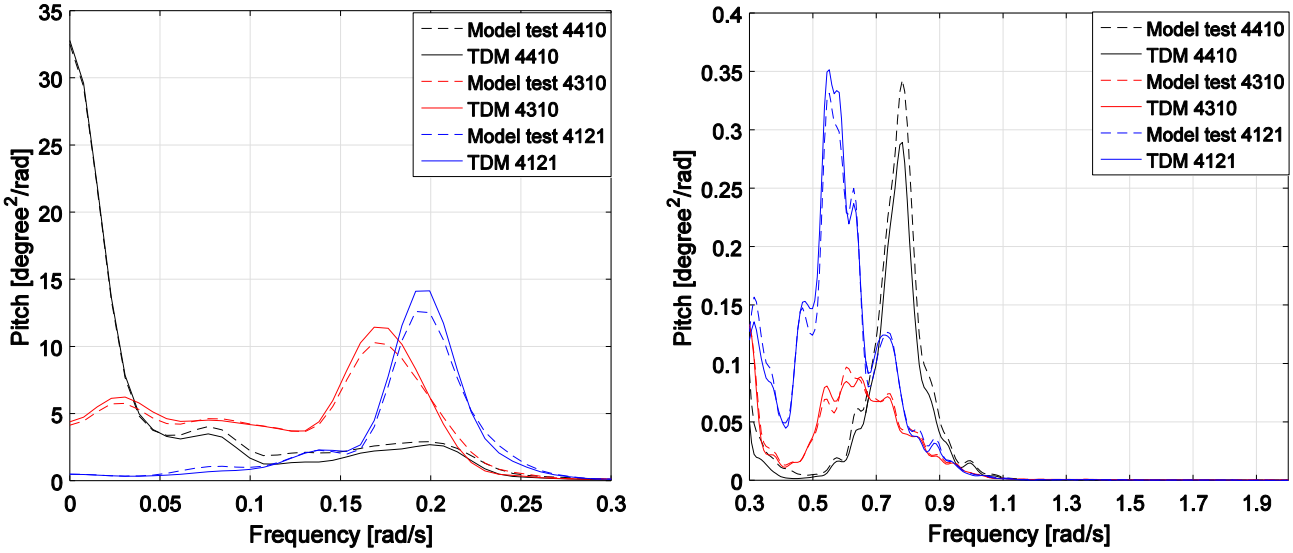

Fig. 5. Comparisons of spectral densities of simulated and measured pitch motions in operational conditions.

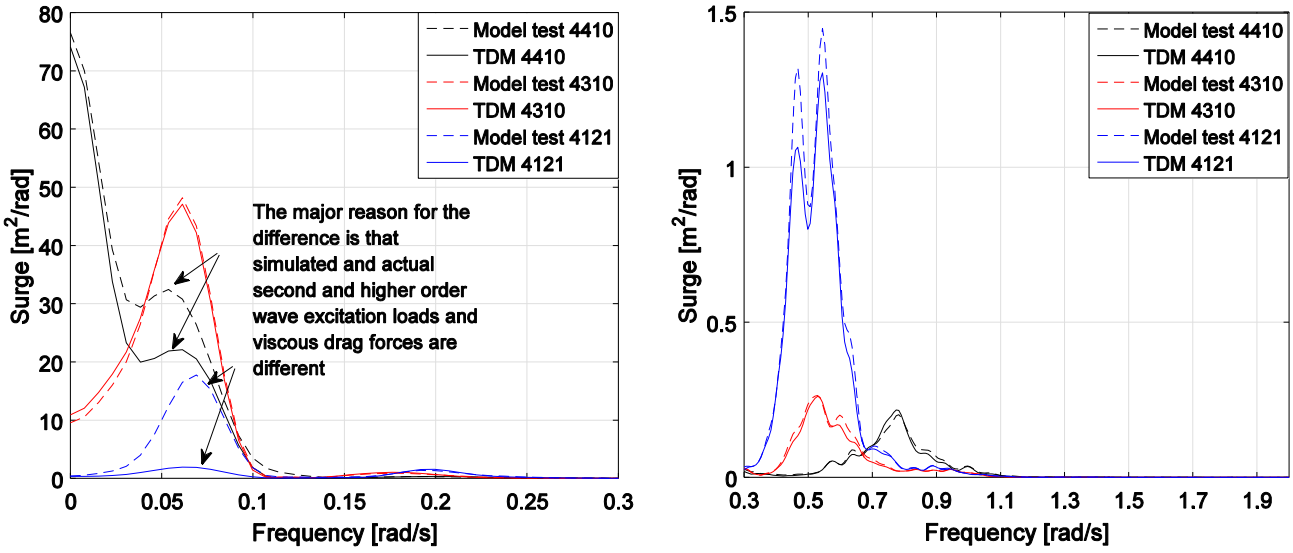

Fig. 6. Comparisons of spectral densities of simulated and measured surge motions in operational conditions.

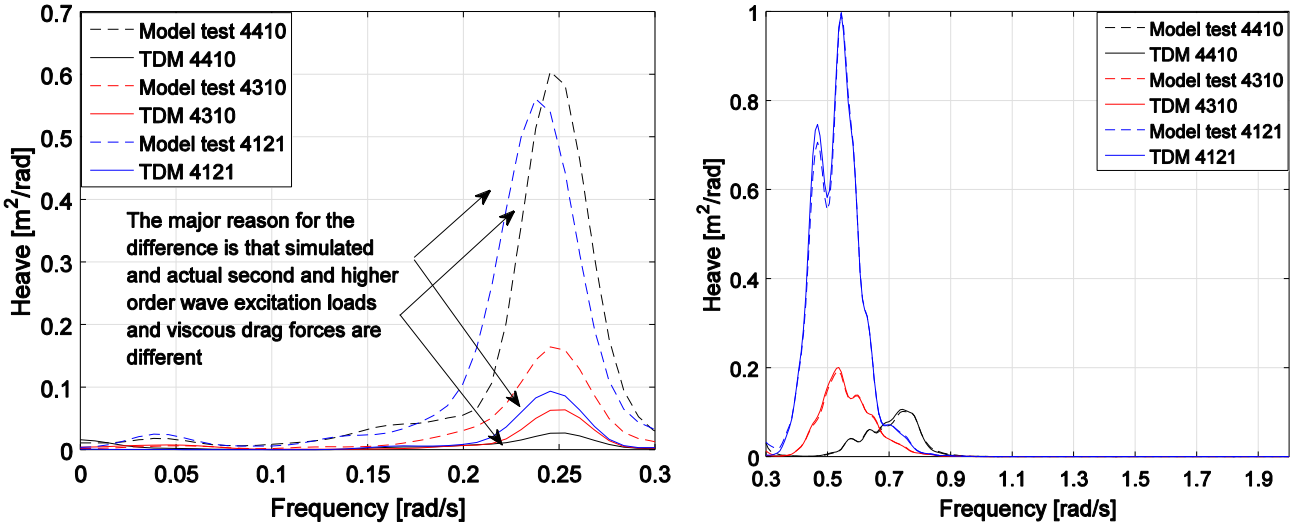

Fig. 7. Comparisons of spectral densities of simulated and measured heave motions in operational conditions.

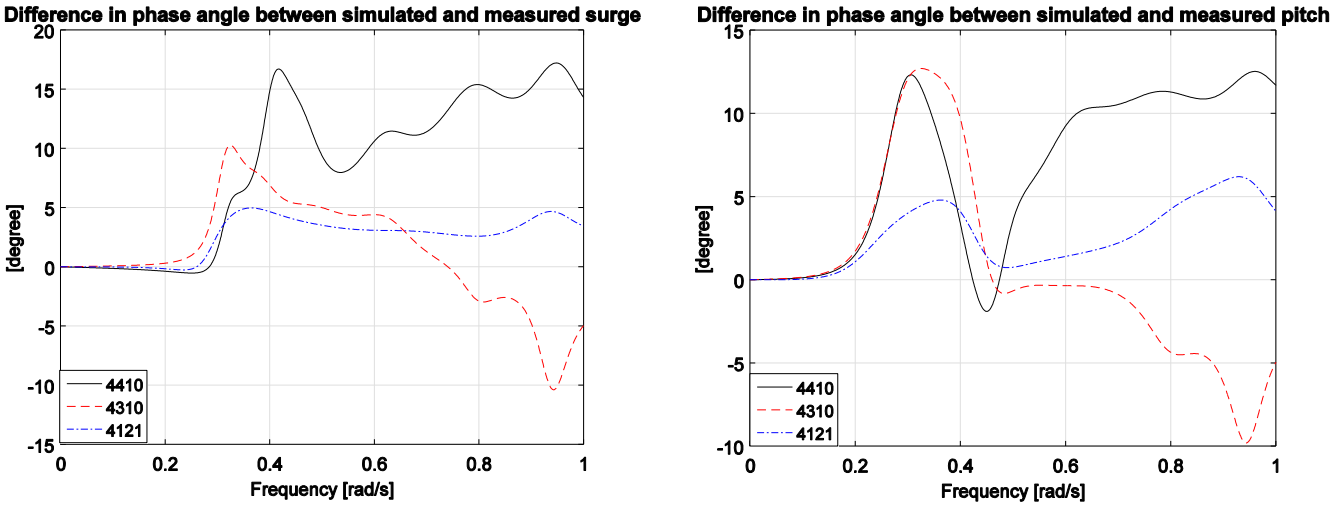

Fig. 8. Difference in phase angle between simulated and measured surge (Left Figure) and pitch (Right Figure) motions in operational conditions.

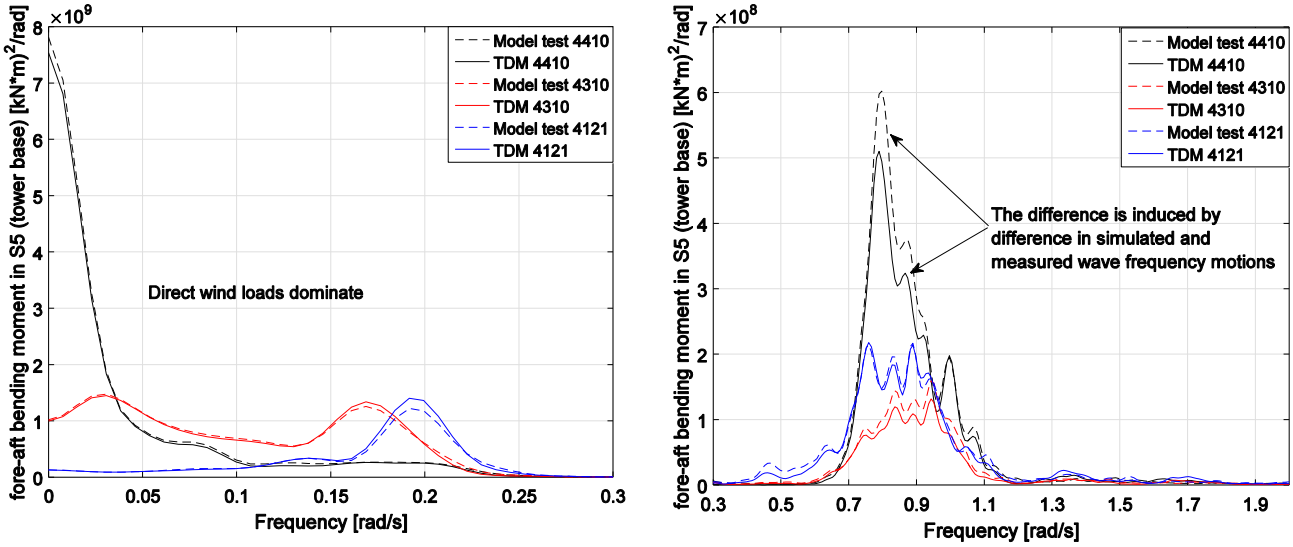

Fig. 9. Comparisons of spectral densities of the simulated and measured fore-aft bending moments in the tower base (S5).

measured pitch motion in low frequency-range is less than 3%, while n_r for standard deviations of the simulated and measured surge motion of the model test 4310 in the low frequency-range is less than 0.34%.

Note that, as shown in Section 3.2, we did not make calibrations with respect to quadratic damping coefficients for the surge motions. This is because that the model tests were not designed for distinguishing the second and higher order wave excitation loads and viscous drag forces from the measured responses. Fortunately, the differences in the surge motions have very limited effects on sectional bending moments.

Comparisons of measured and simulated bending moments are given as follows. More detailed analysis is available later in this paper.

4.2. Comparisons of measured and simulated bending moments in operational conditions

In general, agreement between simulated and measured fore-aft bending moments, in terms of spectral densities and phase angle, is very good. $|n_r|$ for standard deviations of simulated and measured fore-aft bending moments in full frequency-range in the tower base and base of the side column 1 are less than 4% and 10%, respectively. While differences in phase angle between simulated and measured bending moments are no more than 25 degrees, see Figs. 9–13. Mean values of the fore-aft bending moments in the base of the side column (S1) and base of the tower in difference environmental conditions can be significantly different. For instance, mean value of the measured fore-aft bending moment in S1 in the model tests 4121 and 4310 are −2885 kN m and −10,050 kN m. To highlight differences in variations of the measured and simulated fore-aft bending moments in different model tests with respect to time, mean values of realizations presented in Figs. 12 and 13 have been removed. In general, agreement between the simulated and measured mean values of the fore-aft bending moments in S1 and S5 is good and reasonable. For example, relative difference between the simulated and measured mean values of the fore-aft bending moment in S5 is less than −1.3% (the relative difference is only −0.19% in the model test 4310). Mean values of the fore-aft bending moments in S1 are affected by mean components of the second and higher order hydrodynamic loads on the side column 1, e.g. mean wave (drift) forces and moments, which inherently exist in the experimental model test but are not modelled in the numerical models. However, absolute values of the differences between the mean values of simulated and measured fore-aft bending moments in S1 are small and have very limited effect on extreme responses while, roughly speaking, fatigue damage is related to the variations rather than the mean values

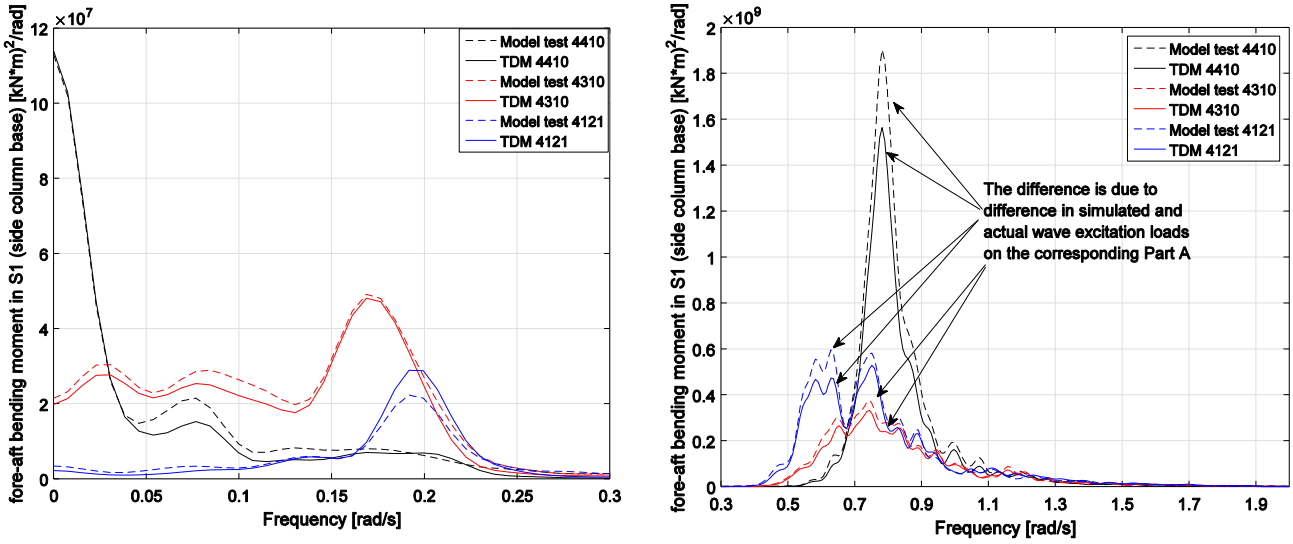

Fig. 10. Comparisons of spectral densities of the simulated and measured fore-aft bending moments in the base of side column 1 (S1).

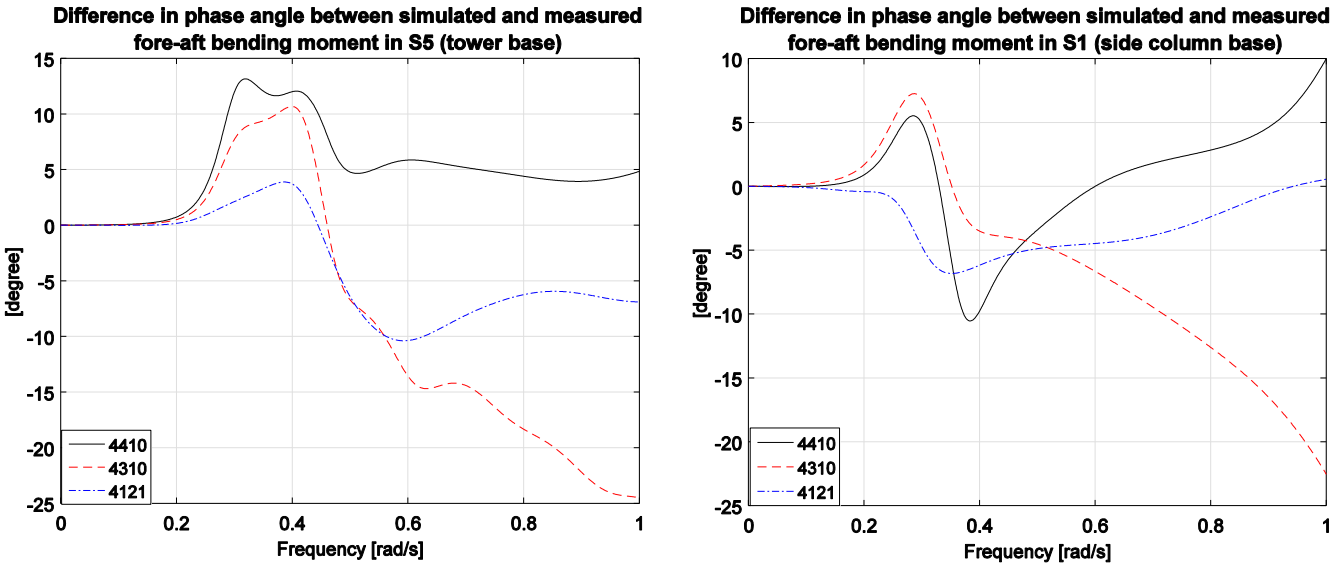

Fig. 11. Differences in the phase angle between simulated and measured fore-aft bending moments in S1 and S5.

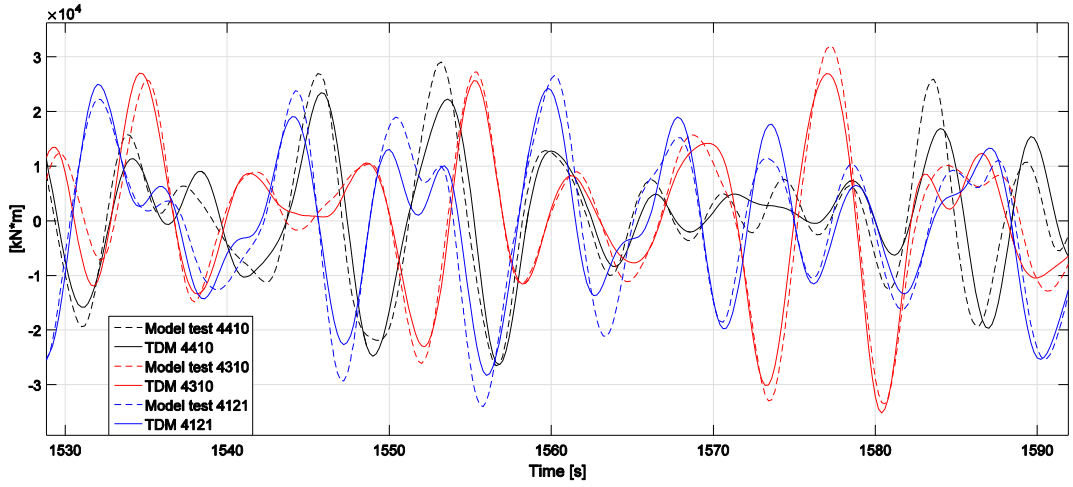

Fig. 12. Comparisons of the simulated and measured realizations of fore-aft bending moments in the base of side column 1 (S1) (mean values have been removed).

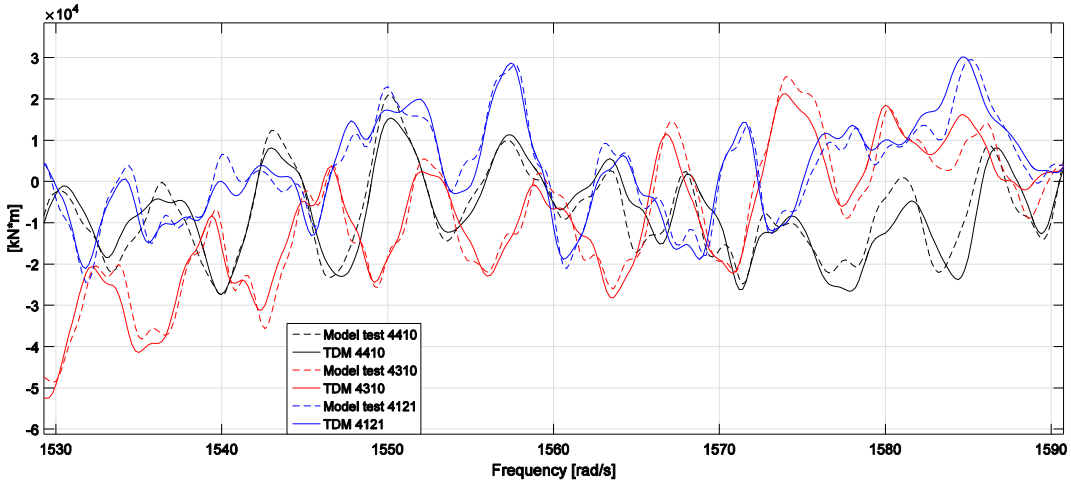

Fig. 13. Comparisons of the simulated and measured realizations of fore-aft bending moments in the base of tower (S5) (mean values have been removed).

of the bending moments. The differences between the mean values of the simulated and measured fore-aft bending moments in S1 in the model tests 4121, 4410 and 4310 are −649 kN m, −714 kN m and −331 kN m, respectively, while simulated 1 h maximum fore-aft bending moments in S1 in these model tests are 51,338 kN m, 49,658 kN m and 29,487 kN m, correspondingly and respectively.

Therefore, in this section, we focus on comparing the differences in standard deviations and spectral densities of the simulations and measurements.

As analyzed in [26], we expect that the differences between the applied aerodynamic loads on the numerical and experimental model are negligible. Major reasons for the difference between wave-frequency components of the simulated and measured bending moments are identified as:

- Differences in the modelled and actual wave excitation loads and radiation loads.
- Differences in the rigid-body motions.

The major reasons for the difference between low frequency components of the simulated and measured bending moments are identified as:

- Differences in the modelled and actual fluctuations of hydrostatic pressure forces and viscous drag forces.
- Differences in the rigid-body motions.

The differences in the rigid-body motions result in differences in the gravity forces and inertial loads on the tower, and the inertial loads and fluctuated hydrostatic pressure forces on the side column 1. To eliminate these differences, the simulations can be modified by regenerating the simulated gravity forces, inertial loads and fluctuated hydrostatic pressure forces by using the measured rigid-body motions instead of using the simulated rigid-body motions.

Comparisons of spectral densities of the simulations with and without the modification and measurements of the fore-aft bending moment in S5 and S1 are given in Figs. 14 and 15, respectively.

In Fig. 14, spectral densities of the simulations with modification are almost identical to the spectral densities of the corresponding measurements. This fact indicates that the differences in the rigid-body motions are the major reason for the differences in simulated and measured fore-aft bending moments in the base of the tower, while the differences in the calibrated and actual moment of inertial of the tower with respect to the tower base is negligible.

In Fig. 15, differences in wave-frequency components of the spectral

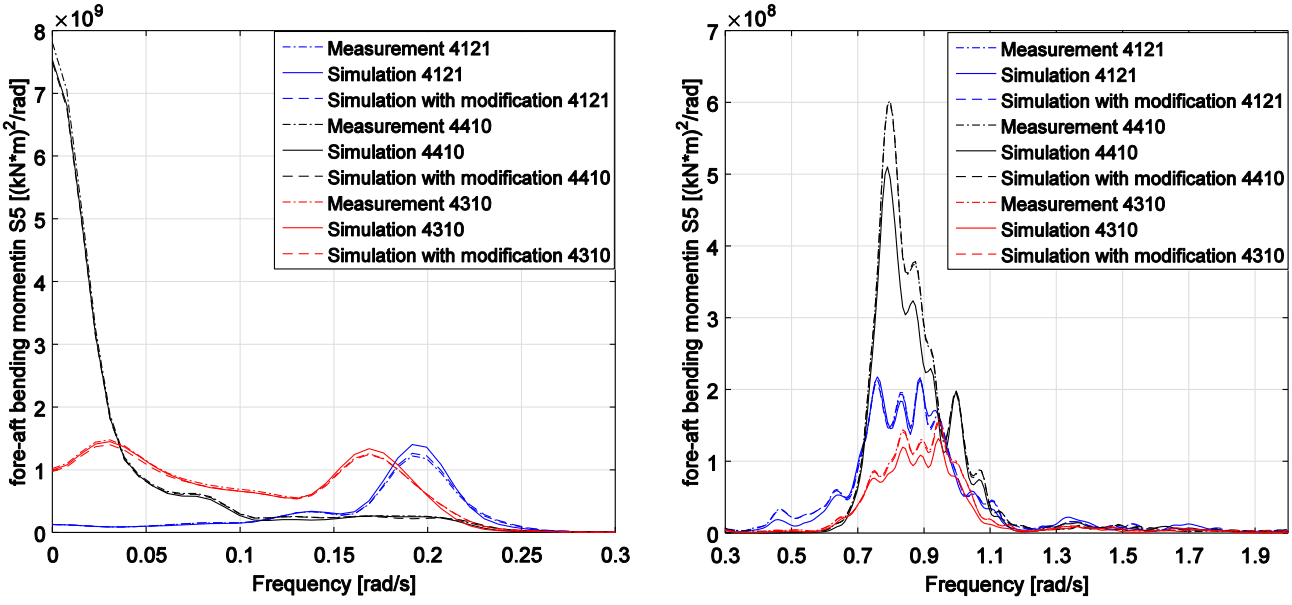

Fig. 14. Comparisons of spectral densities of the simulated and measured fore-aft bending moments in the tower base (S5) with and without the modifications.

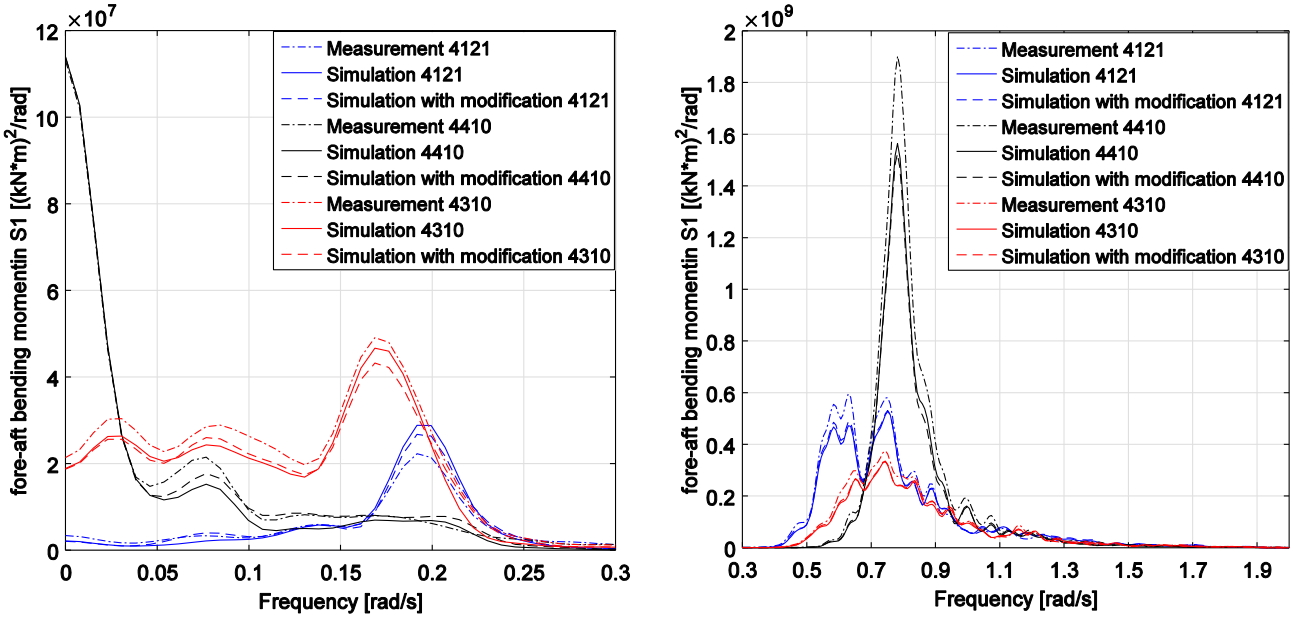

Fig. 15. Comparisons of spectral densities of the simulated and measured fore-aft bending moments in the base of the side column 1 (S1) with and without the modifications.

densities of the simulations with and without the modification are negligible. This indicates that differences exist in the modeled and actual wave excitation loads and radiation loads on the model since these loads dominate the fore-aft bending moments in S1, see discussions in Section 5.2. It should be kept in mind that the second and higher order hydro loads are not completely modeled in the numerical model, however the loads are inherently exist in the experimental model. Sclavounos et al. [36] analyzed non-linear wave excitation loads on a fixed column in a sea state for which the significant wave height is 10.71 m and peak period of the wave spectrum is 15 s. Diameter of the column is 6 meters, which is close to the diameter of the columns of the reference semi-submersible wind turbine. Sclavounos et al. show that the standard deviation of the second order wave excitation loads on the column in surge direction can be approximately 10% of the standard deviation of the first order wave excitation loads. Analyses in Section 5.1 confirm that the experimental model in model tests 4121 and 4410, for which the significant wave heights are 5.9 meters and 5.2 meters respectively, are subjected to considerable non-linear wave excitation loads. The differences in the simulated and actual wave excitation loads agree with, and explain the reason for, the differences observed in the simulated and measured rigid-body motions, see Figs. 5, 6, and 8.

Analysis in Section 5.1 shows that the second and higher order wave excitation loads on the experimental model in the model test 4310, for which the significant wave height is 3.6 meters, are negligible. Consequently, the differences in the simulated and measured results of the model test 4310 are due to the differences in the modeled and actual first order wave excitation loads and radiation loads, and uncertainties and noises in the measurements. Some analysis with respect to the uncertainties and noises are referred to [11] for which the simulated and measured responses of the model in moderate waves, e.g. model test 2420, are analyzed. Note that elevation of incident waves in each model test is measured from its corresponding calibration test which is a repeated test without the experimental model. The model tests 2420 and 4310 correspond to the same calibration test since the incident waves in these model tests are designed to be identical. Differences between measured wave elevations in the calibration test and wave elevations of the actual incident waves in the model tests 2420 and 4310 can be quantified by comparing measurements of these model tests and their repeated tests. The model test 4132 is a repeated test for the model test 4121. Relative difference of standard deviations of measurements of the fore-aft bending moments in full frequency-range in S1of the model tests 4121 and 4132 is 2.48%. Note that repeated tests for the model tests 2420 and 4310, and calibration tests were not carried out. The relative difference of standard deviations of the simulated and measured fore-aft bending moment in the full frequency-range in S1 of the model subjected to environmental conditions of the model tests 4310 and 2420 are 5.3% and 1.4%, respectively. Accounting for the relative difference quantified by the repeated test, the authors feel that the agreements between the measured and simulated fore-aft bending moments in S1 for the model subject to environmental conditions of the model tests 2420 and 4310, respectively, are consistent to each other and acceptable. In addition, note that different sets of coefficients for modeling the first order wave excitation loads and radiation loads are used in the numerical models corresponding to the model tests 4310 and 2420. This is because, from the model test 2420 to the model test 4310, mean configuration of the wetted body surface of the experimental model changes with respect to the mean aerodynamic loads on the tower of the model. More analysis is referred to Section 5.4.

In Fig. 15, for the model test 4310, the differences between the low frequency components of the spectral densities of the simulations with the modification and measurements indicate the differences in the modelled and actual hydrostatic pressure forces on the hull of the model, while the differences in the modelled and actual radiation loads also contribute to the differences in the components with frequencies around the natural frequency of the pitch motion. The differences in the hydrostatic pressure forces are also related to the changes in the mean wetted body surface. More explanation is referred to Section 5.4.

For the model tests 4121 and 4410, some differences in the low frequency components are due to the second and higher order wave excitation loads on the experimental model.

5. Analysis for effect of components on rigid-body motions and sectional bending moments

In this section, effect of the non-linear wave excitation loads, drag forces, each load component, and steady wind and wave loads induced changes with respect to the mean wetted body surface on the rigid-body motions and sectional bending moments are analyzed by comparing the measurements in different conditions and carrying out numerical sensitivity study.

As mentioned in Sections 3.1 and 4, the measured aerodynamic loads are applied on the numerical models. This ensures that the simulated and actual applied aerodynamic loads on the corresponding numerical and experimental models are identical. The differences between the simulated and measured responses are induced by the differences between simulated and actual hydrodynamic loads. As shown in Section 4, in general, agreements between the simulations and measurements are good. This indicates that differences between simulated and actual hydrodynamic loads are small. Consequently, in general, the aerodynamic loads and hydrodynamic loads on the experimental models can be reasonable accounted for in the numerical models. Therefore, the numerical models could be used to analyze the effect of the components on rigid-body motions and sectional bending moments of the 5-MW-CSC.

5.1. Analysis for the effect of the non-linear wave excitation loads and drag forces

Velocity potential can be used to describe unsteady, irrotational and inviscid fluid motion, for which the only external force field is gravity. Consequently, we can consider that the hydro loads are composed of the drag forces due to viscous effects of fluid and potential loads. The potential loads are resultants of pressure forces on the wetted body surface of the hull. We denote position of an arbitrary point on the wetted body surface of the hull in the global coordinate system as (x,y,z). The hydro pressure at the point follows from Bernoulli's equation, see Eq. (3).

$$p = C - \rho g z - \rho \frac{\partial \phi}{\partial t} - \frac{\rho}{2} \nabla \phi \cdot \nabla \phi \tag{3}$$

where ϕ is time dependent velocity potential. C is a constant value related to the atmospheric pressure on free-surface. ρ is density of the sea. g is gravity acceleration.

ϕ is obtained by solving the corresponding boundary value problem [37]. Note that the positions of free-surface and the wetted body surface of the hull in the global coordinate system, and body-velocity are related to the motions of the hull. We define that the wave excitation loads as the potential loads which include ϕ but are independent to the motions of the hull. Rest part of the potential loads is related to the motions of the hull (including first and second derivative of the motions with respect to time).

The drag force on a 2-D cross-section of a structural component, e.g. column, and pontoon, is expressed by Eq. (4), see [5]. v and $\dot{r}$ are corresponding velocities of the fluid and cross-section. $\dot{r}$ can be derived from the motions of the hull. We can see that $L_{drag}^{2D}(v, \dot{r})$ is composed of terms that are related to v^2, $\dot{r}^2$, and $v\dot{r}$. The terms related to v^2 behave as excitation forces while the terms related to $\dot{r}^2$ and $v\dot{r}$ behave as damping forces.

$$L_{drag}^{2D}(v, \dot{r}) = \frac{1}{2}\rho C_D D (v - \dot{r})|v - \dot{r}| \tag{4}$$

Natural periods of the motions of the semi-submersible wind turbine are designed in the low frequency-range to avoid resonances excited by the first order wave excitation loads, while, resonances could be excited by the second and higher order wave excitation loads, excitation loads included in the drag forces, and aerodynamic loads. For wind waves in open sea, significant wave height tends to increase with increase of mean wind speed. This means wave load effect could be more and more important, e.g. effect of the second order wave loads on the motions in the low frequency-range could be more important than the effect of aerodynamic loads. Spectral density curves of the motions and fore-aft bending moments of the experimental model in the extreme and moderate wave only conditions are given in Figs. 16 and 17 and serve as reference values for the motions and sectional forces and moments excited by the second order wave excitation loads in the low frequency-range. The second order wave loads affect the amplitudes and phase angles of the responses of the model.

Measurements in different wind-only and wind and waves conditions are compared as well, see Figs. 16 and 17. Spectral density curves of measurements in the model test 4310 and its corresponding wind-only model test (model test 1713) are almost identical. This indicates that in operational conditions with moderate waves, e.g. the model test 4310, the second and higher order wave excitation loads and drag excitation forces are negligible.

Increased second and higher order wave excitation loads are expected in the model tests 4121 and 4410 as the significant wave height increases. As observed in Fig. 16 the experimental model in the model test 4121 has more low frequency dynamic motions in the surge and heave motions than the one in the corresponding wind-only model test. Another evidence is the differences in spectral densities of the measured fore-aft bending moments in S1 of the model tests 4121 and 1733 (in frequency range from 0 rad/s to 0.15 rad/s).

Note that wave steepness and ratio between water depth and wave length of the measured incident waves in the model tests 4121, 4410 and 4310 indicate that wave crest kinematics of some measured waves are recommended to be modelled by Stokes 2nd order or Stokes 3rd order wave theory [46].

In addition to the low frequency excitation loads, the resonant responses are sensitive to the damping level of the model. Eq. (4) shows that the drag forces on the model include a force that is related to the first derivative of the motions of the hull and fluid velocity ($v\dot{r}$). This indicates that the damping level of the model is related to the incident waves.

The motions of the model in the wind-wave and wind-only conditions are simulated and compared in Fig. 18. The numerical model does not include low frequency wave excitation loads but includes the drag forces. Comparisons of the low frequency components of the simulated motions of the model in the wind-waves and wind-only conditions show

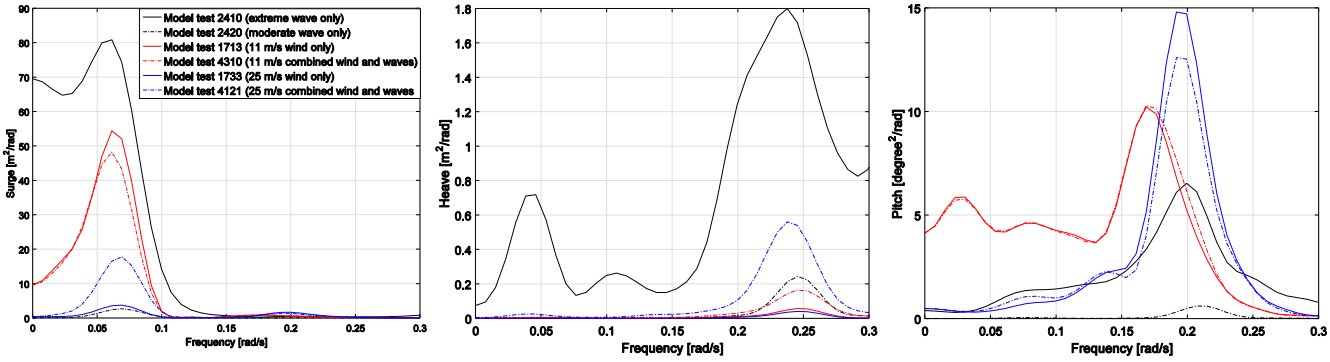

Fig. 16. Comparisons of spectral densities of the measured surge, heave and pitch motions in the wind-only, wave-only and wind-wave conditions.

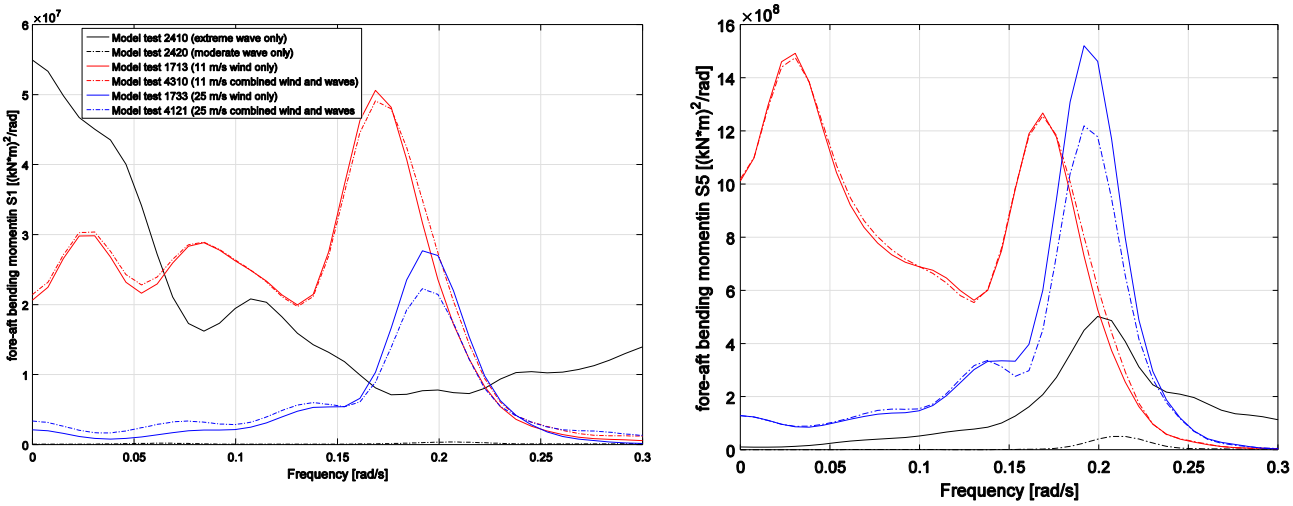

Fig. 17. Comparisons of spectral densities of the measured fore-aft bending moments in S1 and S5 in the wind-only, wave-only and wind-wave conditions.

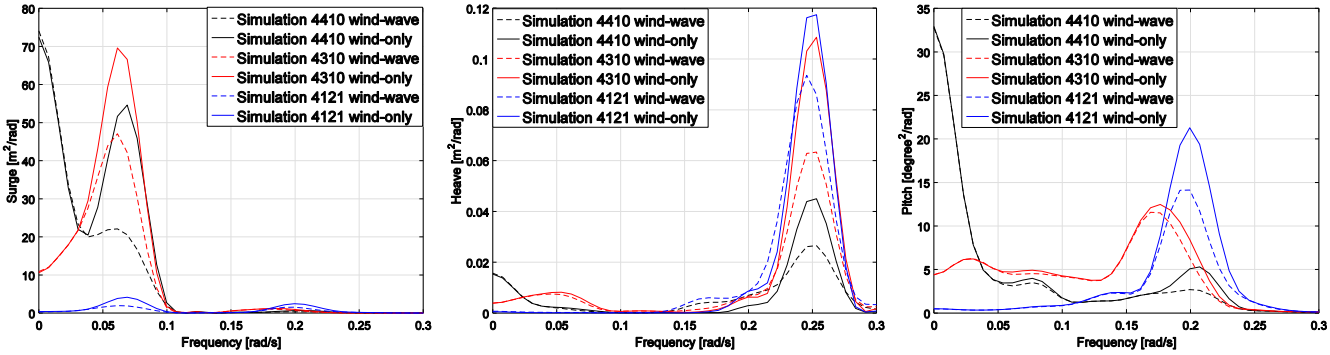

Fig. 18. Comparisons of spectral densities of the simulated surge, heave and pitch motions in the wind-only and wind-wave conditions. Note that the only difference between the numerical model for a wind-wave condition and its corresponding wind-only condition is that the model for the wind-only condition is in calm water.

that the incident waves result in increase of the damping level of the model, while, as a result, the low frequency motions in the frequency ranges around the model's natural frequencies of the surge, heave and pitch motions can be significantly reduced. The observations in Fig. 18 are supported by observations in comparisons of simulations of the conventional numerical models used in [9] for which aerodynamic loads (including aerodynamic damping effect) are accounted for by Aerodyn based on blade element momentum theory.

The differences in spectral densities of measured fore-aft bending moments in S5 and S1 of the model tests 4121 and 1733 (in the frequency range from 0.15 rad/s to 0.25 rad/s) are results of the differences in the pitch motions which are affected by the differences in the damping level and differences in low frequency excitation loads, i.e. 2nd and higher order wave loads and aerodynamic loads, see more discussions in Section 5.2. Effect of the wave excitation loads can be quantified in a straight-forward manner by carrying out a corresponding wave-only model test which is similar as the model tests 2410 and 2420. However, the wave-only model test was not carried out in the laboratory. Analysis and discussions given in this paper are based on available measurements. More systematical model tests are welcome in future.

As shown in Fig. 15 and Table 8, the numerical model based on linear potential-flow theory underestimates the standard deviations of wave-frequency components of the fore-aft bending moments in S1 by 5% to 10%. The differences in the simulated and actual excitation loads are considered as the major reason for the differences. More experimental tests designed for distinguishing linear and non-linear hydro loads are recommended to be considered in future.

5.2. Dominant components in the fore-aft bending moments in five cross-sections

We denote simulated realizations of sectional forces and moments in cross-section SX as $\boldsymbol{R}^{s,SX}(t) = [R_1^{s,SX}, R_2^{s,SX}, R_3^{s,SX}, R_4^{s,X}, R_5^{s,SX}, R_6^{s,SX}]^{\mathrm{T}}$. $\boldsymbol{R}^{s,SX}(t)$ are described in a body-fixed coordinate system ($O^{b,SX}$-$x^{b,SX}$-$y^{b,Sx}$-$z^{b,SX}$) that is identical to the body-fixed coordinate system except that the $O^{b,SX}$ is located at geometrical center of the cross-section SX.

The sectional forces and moments are in equilibrium to external and inertial loads on the corresponding Part A or B. As classified in [9], components of the external loads on Parts A and B are tabulated in Table 9.

Each of the radiation loads ($\boldsymbol{L}^{e,rad,SX,A}(t)$ and $\boldsymbol{L}^{e,rad,SX,B}(t)$, see Table 9) can be expressed as a superposition of a convolution term and a term that is proportional to acceleration associated with the rigid-body motions, see Eq. (5) as an example. In Eq. (5), rigid-body motions are denoted as $\boldsymbol{\eta}^{SX,A}(t)$, $\dot{\boldsymbol{\eta}}^{SX,A}$ and $\ddot{\boldsymbol{\eta}}^{SX,A}$ are first order derivative (velocity) and second order derivative (acceleration) of $\boldsymbol{\eta}^{SX,A}$, respectively. $\boldsymbol{k}_i(t)$ is known as retardation or memory function for Part A and determined by $\boldsymbol{A}_{SX,A}(\omega)$ or $\boldsymbol{B}_{SX,A}(\omega)$. $\boldsymbol{A}_{SX,A}^{\infty}$ is $\boldsymbol{A}_{SX,A}(\omega)$ corresponding to the high-frequency limit. $\boldsymbol{A}_{SX,A}(\omega)$ and $\boldsymbol{B}_{SX,A}(\omega)$ are frequency dependent added mass coefficient matrix and potential damping coefficient matrix for Part A. More details are referred to [9].

$$\boldsymbol{L}^{e,rad,SX,A}(t) = -\int_{-\infty}^{+\infty} \boldsymbol{k}_i^{SX,A}(t-\tau)\dot{\boldsymbol{\eta}}^{SX,A}(\tau)d\tau - \boldsymbol{A}_{SX,A}^{\infty}\ddot{\boldsymbol{\eta}}^{SX,A}(t) \tag{5}$$

Consequently, each realization of simulated sectional forces and

Table 8
Relative difference of standard deviations of the simulated and measured fore-aft bending moments in S1 and S5.

	n_r of Std. of the fore-aft bending moment [%]	Full frequency range	Wave frequency range, in range from 0.3 rad/s to 2 rad/s	Low frequency range, below 0.3 rad/s
S1	4121	−4.6	−4.5	2.8
	4410	−10.2	−10.1	−5.7
	4310	−5.3	−5.2	−4.9
S5	4121	−0.2	−2.2	3.0
	4410	−4.1	−6.8	−2.4
	4310	−2.2	−9.1	−0.3

moments in the specified cross-sections can be expressed as a superposition of realizations tabulated in Table 10. Expression of the superposition is given in Eqs. (6) and (7).

$$\boldsymbol{R}^{s,SX}(t) = \boldsymbol{R}^{waex,SX,A} + \boldsymbol{R}^{flu,SX,A} + \boldsymbol{R}^{Inertia,SX,A} + \boldsymbol{R}^{add_inf,SX,A} + \boldsymbol{R}^{Retard,SX,A} + \boldsymbol{R}^{Res,SX,A}(t),\ SX = 1,\ 2\ or\ 3 \tag{6}$$

$$\boldsymbol{R}^{s,SX}(t) = \boldsymbol{R}^{waex,SX,B} + \boldsymbol{R}^{flu,SX,B} + \boldsymbol{R}^{Inertia,SX,B} + \boldsymbol{R}^{add_inf,SX,B} + \boldsymbol{R}^{Retard,SX,B} + \boldsymbol{R}^{Thrust,SX,B} + \boldsymbol{R}^{Res,SX,B}(t),\ SX = 4\ or\ 5 \tag{7}$$

$\boldsymbol{R}^{s,SX}(t)$ and all of the other terms shown in Eqs. (6) and (7) are simulated in the time-domain model. We focus on fore-aft bending moments ($R_5^{s,SX}$) which are the sectional bending moments with respect to axis $y^{b,Sx}$ and intend to identify dominant terms in the fore-aft bending moment.

Spectral density functions of $R_5^{s,SX}$ and different combinations of the corresponding terms are compared.

For example, according to Eq. (7), we have Eq. (8). As shown in Fig. A4, the spectral density curves of $R_5^{s,S5}$ and $R_5^{flu,S5,B} + R_5^{Thrust,S5,B}$ are almost identical in the frequency-range from 0 rad/s to 0.1 rad/s. This indicates that effects of $R_5^{Inertia,S5,B}$ on $R_5^{s,S5}$ are negligible in this frequency-range.

Note that $\boldsymbol{R}^{flu,S5,B}$, gravity forces and hydrostatic pressure forces on the Part B (the tower and RNA) corresponding to the cross-section S5 (the tower base) are in equilibrium. Similarly, $\boldsymbol{R}^{Thrust,S5,B}$ and $\boldsymbol{R}^{Inertia,S5,B}$ are in equilibrium to the applied thrust forces and moments (aerodynamic loads) and inertia loads on the corresponding Part B, respectively. For S5, there are no hydro pressure forces on the Part B since the Part B is out of the sea. Consequently, $\boldsymbol{R}^{flu,S5,B}$ is, actually, in equilibrium to the gravity forces. Meanwhile, $\boldsymbol{R}^{waex,S5,B}$, $\boldsymbol{R}^{add_inf,S5,B}$ and $\boldsymbol{R}^{Retard,S5,B}$, which are in equilibrium to hydrodynamic pressure forces on the corresponding Part B are not exist. Except for the external and inertia loads on the Part B discussed in above the numerical models do not have any other external and/or inertial loads on the Part B. Consequently, $\boldsymbol{R}^{Res,S5,B}$ does not exist.

$$R_5^{s,S5}(t) = R_5^{flu,S5,B} + R_5^{Inertia,S5,B} + R_5^{waex,S5,B} + R_5^{add_inf,S5,B} + R_5^{Retard,S5,B} + R_5^{Thrust,S5,B} + R_5^{Res,S5,B} = R_5^{flu,S5,B} + R_5^{Inertia,S5,B} + R_5^{Thrust,S5,B} \tag{8}$$

Using this approach, dominant components in the fore-aft bending moments in five cross-sections are analysed. Results are summarized in Table 11.

In the numerical models, $\boldsymbol{R}^{Thrust,SX,B}$, $\boldsymbol{R}^{waex,SX,B}$ and $\boldsymbol{R}^{waex,SX,A}$ are prescriptive since the thrust forces and moments applied on the numerical models are identical to the measurements of the thrust forces and moments applied on the experimental model during the model tests, while the first-order wave loads are generated based on the corresponding hydrodynamic coefficients, which are related to configuration of the mean wetted body surface of the hull and obtained by solving the corresponding boundary value problem [9] and measured wave elevations of incident waves.

$\boldsymbol{R}^{Inertia,SX,A}$ and $\boldsymbol{R}^{Inertia,SX,B}$ are related to mass distributions of the hull and the acceleration associated with rigid-body motions. $\boldsymbol{R}^{add_inf,SX,A}$ and $\boldsymbol{R}^{add_inf,SX,B}$ are related to the acceleration associated with the rigid-body motions and configuration of the mean wetted body surface of the hull.$\boldsymbol{R}^{flu,SX,A}$ and $\boldsymbol{R}^{flu,SX,B}$ are related to rigid-body motions, distribution of the vertical position of the mass of the hull and

Table 9
List of the components of external loads on Parts A and B.

Components (Each component is 6 × 1 vector including three forces and moments)	On Part A corresponding to SX	On Part B corresponding to SX
Drag forces	$\boldsymbol{L}^{e,vis,SX,A}(t)$	$\boldsymbol{L}^{e,vis,SX,B}(t)$
Gravity loads	$\boldsymbol{L}^{e,gra,SX,A}(t)$	$\boldsymbol{L}^{e,gra,SX,B}(t)$
First order wave excitation loads	$\boldsymbol{L}^{e,waex,SX,A}(t)$	$\boldsymbol{L}^{e,waex,SX,B}(t)$
First order radiation loads	$\boldsymbol{L}^{e,rad,SX,A}(t)$	$\boldsymbol{L}^{e,rad,SX,B}(t)$
Resultant forces and moments of hydrostatic pressure forces on the outer surface and the atmospheric pressure forces on the inner surface of the corresponding part (the corresponding Part A or B) at instantaneous position	$\boldsymbol{L}^{e,sta,SX,A}(t)$	$\boldsymbol{L}^{e,sta,SX,B}(t)$
Applied thrust forces and moments	Not applicable	$\boldsymbol{L}^{e,thrust,SX,B}(t)$

Table 10
List of decomposed realizations of the simulated sectional forces and moments. All the terms in Eqs. (6) and (7) are described in the body-fixed coordinate system ($\boldsymbol{O^{b,SX}}$-$\boldsymbol{x^{b,SX}}$-$\boldsymbol{y^{b,Sx}}$-$\boldsymbol{z^{b,SX}}$) with respect to $\boldsymbol{O^{b,SX}}$.

Realizations in Eq. (6)	Definition
$\boldsymbol{R}^{waex,SX,A}$	Simulated realizations of three forces and moments that are in equilibrium to $\boldsymbol{L}^{e,waex,SX,A}$
$\boldsymbol{R}^{flu,SX,A}$	Simulated realizations of three forces and moments that are in equilibrium to $\boldsymbol{L}^{e,gra,SX,A}$ and $\boldsymbol{L}^{e,sta,SX,A}$
$\boldsymbol{R}^{Inertia,SX,A}$	Simulated realizations of three forces and moments that are in equilibrium to inertial loads of corresponding Part A
$\boldsymbol{R}^{add_inf,SX,A}$	Simulated realizations of three forces and moments that are in equilibrium to $-\boldsymbol{A}_{SX,A}^{\infty}\ddot{\boldsymbol{\eta}}^{SX,A}$
$\boldsymbol{R}^{Retard,SX,A}$	Simulated realizations of three forces and moments that are in equilibrium to the convolution term $(-\int_{-\infty}^{+\infty}\boldsymbol{k}_i^{SX,A}(t-\tau)\dot{\boldsymbol{\eta}}^{SX,A}(\tau)d\tau)$
$\boldsymbol{R}^{Res,SX,A}$	Simulated realizations of three forces and moments that are in equilibrium to the rest external loads on the corresponding Part A, e.g. $\boldsymbol{L}^{e,vis,SX,A}$
Realizations in Eq. (7)	Definition
$\boldsymbol{R}^{Thrust,SX,B}$	Simulated realizations of three forces and moments that are in equilibrium to $\boldsymbol{L}^{e,thrust,SX,B}$
Similarly, $\boldsymbol{R}^{waex,SX,B}$, $\boldsymbol{R}^{flu,SX,B}$, $\boldsymbol{R}^{Inertia,SX,B}$, $\boldsymbol{R}^{add_inf,SX,B}$, $\boldsymbol{R}^{Retard,SX,B}$ and $\boldsymbol{R}^{Res,SX,B}$ are in equilibrium to the corresponding loads on the corresponding Part B	

Table 11
Summary of dominant load components in the fore-aft bending moments in the five cross-sections.

	Low frequency-range			Wave-frequency-range	
	Around surge natural frequency	Around pitch natural frequency			
	0–0.05 rad/s	0.05–0.15 rad/s	0.15–0.25 rad/s	0.25–0.3 rad/s	0.3–2 rad/s
S1	$R_5^{flu,SX,A}$, X = 1, 2or3		$R_5^{flu,SX,A} + R_5^{Inertia,SX,A} + R_5^{add_inf,SX,A}$, X = 1, 2or3	Components of $R_5^{s,SX}$, X = 1, 2, 3, 4or5 in this range are negligible since excitations and rigid-body motions in this range are very limited.	$R_5^{waex,S1,A} + R_5^{Inertia,S1,A} + R_5^{add_inf,S1,A}$ $R_5^{waex,SX,A} + R_5^{Inertia,SX,A} + R_5^{add_inf,SX,A} + R_5^{flu,SX,A}$, X = 2or3
S2					
S3					
S4	$R_5^{flu,SX,B} + R_5^{Thrust,SX,B}$, X = 4or5		$R_5^{flu,SX,B} + R_5^{Thrust,SX,B} + R_5^{Inertia,SX,B} + R_5^{add_inf,SX,B}$, X = 4or5		$R_5^{waex,S4,B} + R_5^{Inertia,S4,B} + R_5^{add_inf,S4,B} + R_5^{Thrust,S4,B} + R_5^{flu,S4,B}$
S5					$R_5^{flu,S5,B} + R_5^{Inertia,S5,B} + R_5^{Thrust,S5,B}$

configuration of the mean wetted body surface of the hull.

In the numerical models, the dynamic motions and sectional forces and moments in the hull are excited by the first-order wave loads and thrust forces and moments, which are dominant excitations for the wave frequency responses and low frequency responses, respectively. Components of the fore-aft bending moments with oscillating frequencies in range from 0.25 rad/s to 0.3 rad/s are negligible since excitations and rigid-body motions in this range are very limited.

For a model oscillating with frequency ω_0, inertial loads of the model are proportional to ω_0^2. Therefore, effects of $\boldsymbol{R}^{Inertia,SX,A}$, $\boldsymbol{R}^{Inertia,SX,B}$, $\boldsymbol{R}^{add_inf,SX,A}$ and $\boldsymbol{R}^{add_inf,SX,B}$ on components of the fore-aft bending moments with very small oscillating frequencies, e.g. below 0.05 rad/s, are negligible when compared to the corresponding $\boldsymbol{R}^{Thrust,SX,B}$, $\boldsymbol{R}^{flu,SX,A}$ and $\boldsymbol{R}^{flu,SX,B}$ even though in nature large low-frequency motions, e.g. the surge and pitch motions, may be excited by wind loads on the RNA and tower, and second and higher order wave excitation loads on the hull. For the reference semi-submersible wind turbine, we observe that components of the fore-aft bending moments with oscillating frequencies in the low frequency-range are dominated by $R_5^{flu,SX,A}$ or $R_5^{flu,SX,B} + R_5^{Thrust,SX,B}$ except that inertial related terms, e.g. $R_5^{Inertia,SX,A}$ and $R_5^{add_inf,SX,A}$, can affect the components of the fore-aft bending moments with oscillating frequencies that are around pitch and surge natural frequencies since 1) amplitudes of rigid-body motions are amplified as the resonant motions are excited, and 2) $R_5^{flu,SX,A}$, $R_5^{flu,SX,B}$, $R_5^{Thrust,SX,B}$ and the terms related to the acceleration associated with the rigid-body motions are not uncorrelated.

The resonant rigid-body motions are sensitive to the level of the damping forces. Consequently, rigid-body-motion related terms of $\boldsymbol{R}^{s,SX}$, e.g. $\boldsymbol{R}^{flu,SX,A}$, $\boldsymbol{R}^{Inertia,SX,A}$ and $\boldsymbol{R}^{add_inf,SX,A}$, are sensitive to the level of the damping forces. While, a numerical sensitivity analysis shows that the fore-aft bending moments, which are in the five cross-sections and in equivalent to the corresponding damping forces on the corresponding Part A or B, are negligible when compared to $\boldsymbol{R}^{s,SX}$. It should be noted that, as discussed in Section 5.1, the damping forces and moments are affected by incident waves via the term $v\dot{r}$.

Relative importance of load components on the fore-aft bending moments depends on wind and wave conditions, location of the cross-section in the hull, amplitudes and phase angles of the rigid-body motions, and configuration of corresponding wetted body surface of the hull, as well. Effect of these issues is analyzed in Sections 5.3–5.5.

5.3. Comparisons of the simulated fore-aft bending moments in the specified five cross-sections

Spectral densities of the fore-aft bending moments in the five cross-sections for the model in the three wind-wave environmental conditions are compared, see Fig. 19. The interface between the pontoons and central column is identified as the most critical structural component. Ratio between square root of area under low frequency-range and wave-frequency-range of each spectral density curve is calculated. We find the ratio varies from 0.1, which means the corresponding fore-aft bending moment is dominated by wave frequency components (see the bending moment in S1), to 2.3, which means the corresponding bending moment is dominated by low frequency components (see the bending moment in S5 in the model tests 4310 and 4410). The ratio is around 1 for the corresponding bending moment in S5 in the model test 4121, S2, S3 and S4. This indicates that both of the low frequency and wave frequency components are important.

Spectral densities of $R_5^{waex,SX,A}$, $(R_5^{Inertia,SX,A} + R_5^{add_inf,SX,A})$ and $R_5^{flu,SX,A}$, X = 1, 2or3, $R_5^{waex,S4,B}$, and $(R_5^{Inertia,SX,B} + R_5^{add_inf,SX,B})$ and $R_5^{flu,SX,B}$ are compared. See Fig. 20 for example. From S1 to S3, value of standard deviation of the corresponding first order wave excitation load induced fore-aft bending moment increases. Effects of fluctuation of hydrostatic pressure forces on wetted body surface of the hull and fluctuation of gravity forces are important to fore-aft bending moments

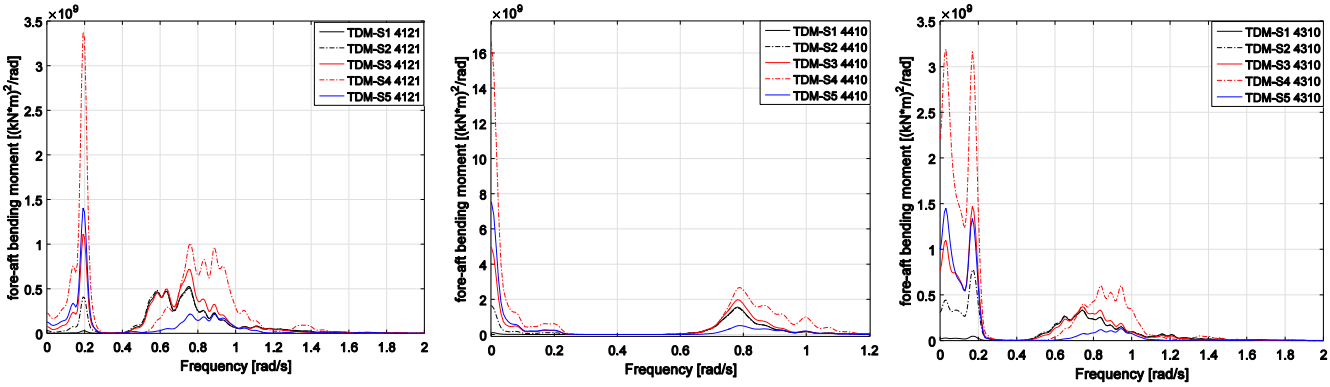

Fig. 19. Comparisons of spectral densities of the simulated fore-aft bending moments in the five cross-sections in the three wind-wave conditions.

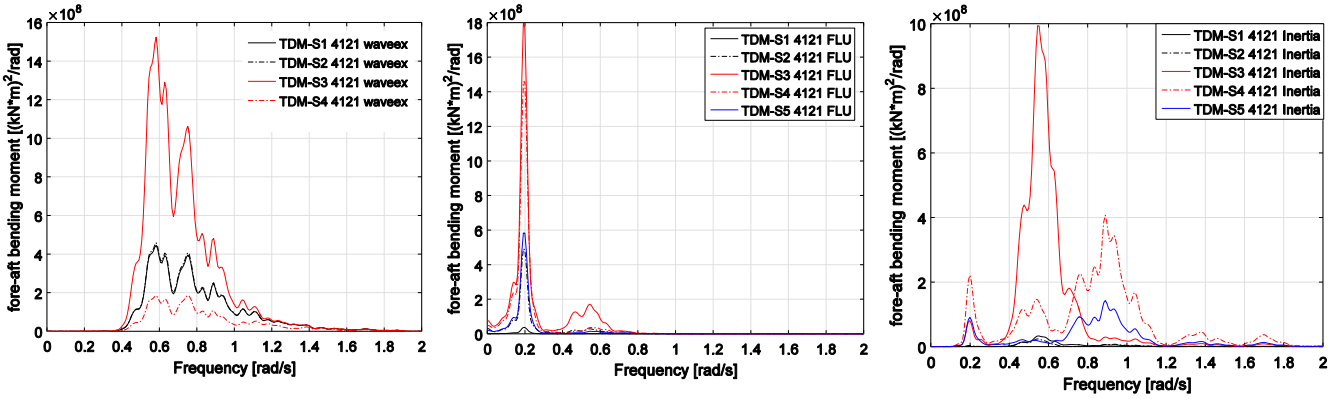

Fig. 20. Comparisons of spectral densities of $\boldsymbol{R}^{waex,SX,A}$ (waveex), $\boldsymbol{R}^{flu,SX,A}$ (FLU) and $\boldsymbol{R}^{Inertia,SX,A} + \boldsymbol{R}^{add_inf,SX,A}$ (Inertia), $X = 1, 2 or 3$, and $\boldsymbol{R}^{waex,SX,B}$, $\boldsymbol{R}^{flu,SX,B}$ and $\boldsymbol{R}^{Inertia,SX,B} + \boldsymbol{R}^{add_inf,SX,B}$, $X = 4 or 5$.

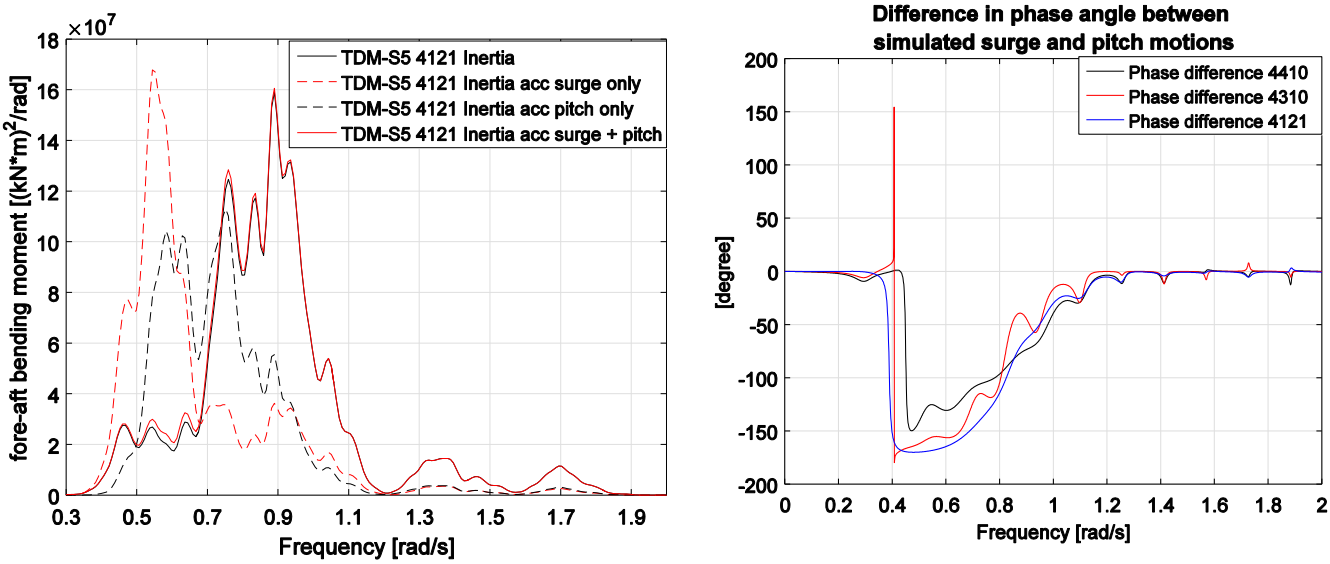

Fig. 21. Left: comparisons of spectral densities of the simulated fore-aft bending moments in S5 which are in equivalent to different components of the inertial loads of the RNA and tower; right: differences in phase angle between simulated surge and pitch motions.

in cross-sections in the tower and central column and in cross-sections that are on the pontoons and close to the central column.

The inertial loads induced fore-aft bending moments in the tower base and base of the central column are dominated by the inertial loads that are proportional to the acceleration associate with the surge and pitch motions. Spectral densities of the fore-aft bending moments in the tower base, which are in equilibrium to the components of the inertial loads on the tower that are associated to acceleration in surge only, acceleration in pitch only and acceleration in combined surge and pitch, are given in the left figure of Fig. 21. A cancellation effect between the bending moments induced by the inertial loads that are associated to acceleration in surge and pitch can be clearly observed in frequency range from 0.4 rad/s to 0.6 rad/s. The cancellation is due to, as shown by the right figure given in Fig. 21, the fact that phase difference between simulated surge and pitch motions is close to 180 degrees in this frequency range.

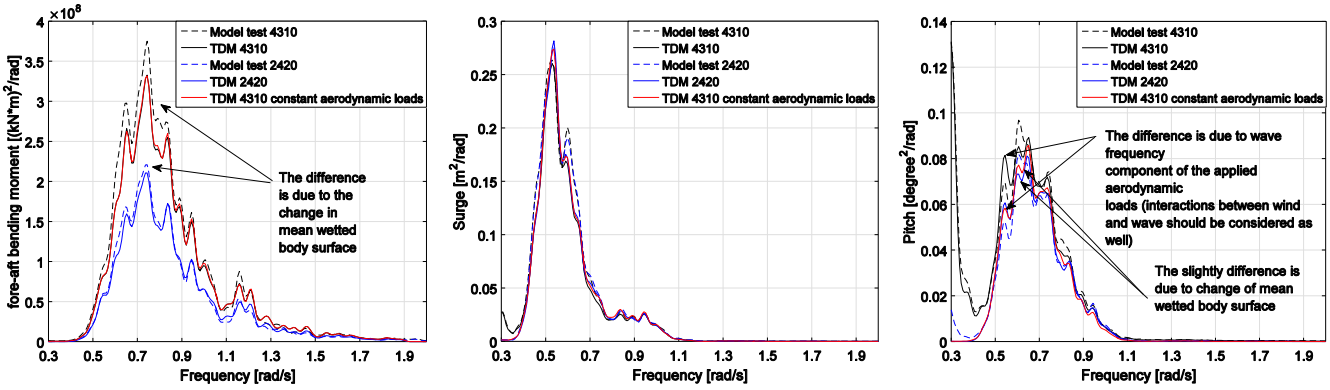

Fig. 22. Comparison of spectral densities of the simulated and measured fore-aft bending moments in S1, and the surge and pitch motions. The model test 4310 is a combined wind-wave condition, while the model test 2420 is its corresponding wave only condition.

By using the same analysis approach, we find that the inertial loads induced fore-aft bending moments in S3 are dominated by the inertial loads that are proportional to the acceleration associate with the heave motions.

5.4. Analysis for effects of changes in the mean-offset and mean-heeling-angle of the hull on rigid-body motions and sectional bending moments

As mentioned in Section 3, floating wind turbines are subjected to constant forces and moments from wind and waves. These constant forces and moments can result in a mean horizontal offset and title angle. The horizontal offset results in a change in restoring stiffness of the mooring lines due to change in configuration of the mooring lines and a change in phase angle of each frequency component of the incident waves. As shown in Fig. 3, the tilt angle means a change in configuration of mean wetted body surface of the hull which results in a change in corresponding velocity potential and a change in value and distribution of hydro pressure forces on the wetted body surface. This may result in a considerable change in resultant sectional forces and moments even though change in resultant of the hydro pressure forces on whole of the wetted body surface could be very limited. This statement is substantiated by comparisons of the measurements and simulations of the platform in a combined wind-wave condition (the model test 4310), its corresponding wave only condition (model test 2420), and a model for which averaged wind induced forces and moments are applied, see Fig. 22.

5.5. Convolution terms in expressions of the radiation loads

It is of great interesting to analyze load effects of the convolution terms shown in the expressions of $\boldsymbol{L}^{e,rad,SX,A}$ and $\boldsymbol{L}^{e,rad,SX,B}$ since computational cost and complexity of the numerical models can be significantly reduced if the convolution terms can be neglected. $\boldsymbol{R}^{Retard,SX,A}$ and $\boldsymbol{R}^{Retard,SX,B}$ are in equilibrium to the corresponding convolution terms, respectively. Comparisons of the numerical results presented in Section 5.2 show that $R_5^{Retard,SX,B}$, $X = 4\text{or}5$, and $R_5^{Retard,SX,A}$, $X = 1, 2\text{or}3$, are negligible for the analyzed model.

Spectral densities of the rigid-body motions and fore-aft bending moments in the five cross-sections given by numerical models with and without the convolution terms in the expressions of radiation loads on each part of the hull are compared, see Appendix B. Numerical model without the convolution terms means that 1) the potential damping forces are not modelled, and 2) the frequency dependent added mass coefficients are replaced by added mass coefficients that corresponding to the high-frequency limit. Components of the potential damping forces with oscillating frequencies in the low frequency range are expected to be negligible. We find that effect of the convolution terms on the motions and fore-aft bending moments of the present model in the analyzed environmental conditions are negligible. This is agreed by the measured responses and indicates that, for the analyzed environmental conditions, Morsion formula with calibrated coefficients could be available to reasonably account for the hydro dynamic loads on the hull. However, this should be validated in future. By now, computer codes which implement Morison formula focus on rigid-body motions while thorough validation with respect to sectional forces and moments in semi-submersible wind turbine hulls is very limited. In addition, as addressed in [8], hydro pressure forces on end surface of each structural component of floating wind turbine hulls need to be appropriately accounted for in the computer codes which implement Morison formula.

Note that importance of the convolution terms is related to configurations of the wetted body surface, and amplitudes and frequencies of the motions of the hull. According to potential flow theory, it is expected that the effect of the convolution terms on the dynamic responses of the 5-MW-CSC could be more important when the model is subjected to waves with smaller periods, e.g. below 8 s. This effect needs to be considered in design of model test in future. It is also of great interest to apply the Luan et al.'s approach on numerical and experimental analysis of a floater with large water plane area for which the convolution terms could be important.

In contrast to using Morison formula to model the hydrodynamic loads on floaters, hydrodynamic coefficients used in the Luan et al.'s approach are obtained by solving the corresponding boundary value problem (there is no need to calibrate the hydrodynamic coefficients). While, the Luan et al.'s approach is expected to be available in situations for which the diffraction and radiation effects are important, e.g. for waves with relatively small periods.

6. Simplification of numerical modelling for global dynamic analysis

Interaction effect between wind and wave loads may be very limited while the interaction effect on the sectional forces and moments may be negligible.

For example, as shown in Fig. 17, the low frequency components of spectral densities of the measured fore-aft bending moments in the tower base (S5) and base of the side column 1 (S1) in the model test 4310, for which the model is subjected to turbulent winds and moderate irregular waves, are almost identical to the low-frequency components of spectral densities of the corresponding measurements in the model test 1713 which is a wind-only model test corresponding to the model test 4310. While the interaction effect can be observed from the differences between the wave frequency components of spectral densities of simulated pitch motions in environmental condition of the model test 4310 and the model test for which the model is subjected to the same condition as the model test 4310 except that the corresponding applied aerodynamic load, which include wave frequency

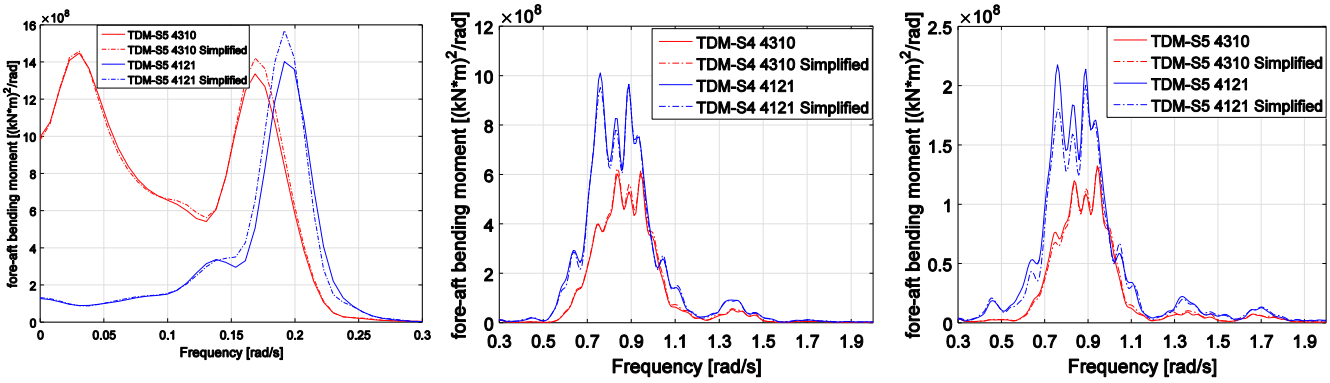

Fig. 23. Comparisons of spectral densities of simulated fore-aft bending moments with and without the simplification for two operational conditions.

components, are replaced by three constant forces and moments that are averaged wind induced forces and moments (constant steady wind loads), see Fig. 22. However, as shown in Fig. 22, the differences between the wave frequency components of the spectral densities of the simulated fore-aft bending moment in S1 in these two conditions are negligible. This is because that the wave frequency components of the fore-aft bending moments in S1 are dominated by the wave excitation loads and inertial and radiation loads which are related to wave induced motions.

These facts encourage the idea that the fore-aft bending moments of the model in wind and waves could be approximately but effectively simulated by superimposing the corresponding simulations of the model subjected to its corresponding wind only condition and wave only condition with the corresponding averaged wind induced forces and moments. If the simplification is applicable, the number of cases of short-term analysis required in long-term analysis can be significantly reduced. In addition, based on the results discussed in Section 5.5, we suggest that the convolution terms could be excluded from the numerical model to reduce real-time-computational effort and modelling complexity for each short-term analysis. Consequently, the computational time for a 4600-s-simulation can be reduced from 1253 s to 638 s (for a 2.30 GHz CPU). Note that effect of the convolution terms on responses of a generic floater could be important if the floater has relatively large volume of displaced water and/or is subjected to waves with relatively small wave length.

Applicability of the simplification should be analyzed case by case. Spectral densities of the simulated fore-aft bending moments in the five cross-sections of the models with and without the simplification in conditions of the model tests 4310 and 4121 have been compared. Typical results are shown in Fig. 23. As expected, these results substantiate that the simplification could be used to simulate the fore-aft bending moments in the hull. Relative difference between square root of area of corresponding spectral density curves with and without the simplification under the low frequency-range and wave-frequency-range are no more than 2.5% and 5%, respectively. We also find that fore-aft bending moments in cross-sections in the tower could be sensitive to the difference in the simulated pitch motion and thrust force on the rotor with and without the simplification but could be insensitive to the difference in the simulated surge motion. Fore-aft bending moments in cross-sections in the side columns could be insensitive to the difference in the simulated motions and thrust force on the rotor since the fore-aft bending moments are dominated by wave excitation loads, and inertial and radiation loads which are related to wave induced motions.

Note that the simulated model responses in the frequency-range around surge and pitch natural frequencies are very sensitive to damping level of the numerical model. In the numerical models, the damping forces and moments in the low frequency-range come from 1) drag forces on the mooring lines and hull and 2) the quadratic damping matrix. Morison formula, which is an empirical formula, is used to model the drag forces. The coefficients implemented in the formula are selected according to [31] based on Reynolds number, Keulegan–Carpenter number and surface roughness of the model in full size. As shown in Section 5.1, due to implementation of the Morison formula, incident waves can introduce a considerable effect on the damping level of the numerical model in the low frequency-range. Consequently, drag coefficients calibrated by using measured responses in decay tests and/or selected according to standards, e.g. [31], may failed to accurately model the actual drag forces (value and distribution) on the hull and mooring lines. In practice, a quadratic damping matrix is used to compensate the difference between the model and actual damping forces and moments. However, calibration for coefficients in the quadratic damping matrix is needed case by case. Future work for improving the modelling approach for the drag forces is highly recommended. In addition, the second and higher order hydro loads are not completely included in the numerical models but are inherently included in nature. Effect of the second and higher order wave excitation loads on the resonant motions should be kept in mind. As shown by the measured responses of the model test 4310, in moderate waves, effect of the second and higher order hydro loads is very limited.

7. Conclusions and future work

Multi-body time-domain finite element models, which implement a recently developed numerical approach for determining forces and moments in floaters, are developed to simulate rigid-body motions and sectional forces and moments of a reference 5-MW braceless semi-submersible wind turbine in turbulent winds and irregular waves corresponding to below rated, at rated and above rated conditions. The simulated responses are compared with measurements with a 1:30 scaled model test. In general, the agreement between the simulations and measurements is very good. The differences in the spectral densities of the measurements and simulations have been quantified while the reasons for the differences have been thoroughly analyzed and discussed based on the comparisons of measurements in the different conditions and numerical parametrical study.

The low frequency rigid-body motions are dominated by the wind loads, second and higher order wave excitation loads, and restoring stiffness while the resonant motions are sensitive to the damping forces and moments that are empirically modeled by the drag terms of the Morison formula in the developed numerical models and are affected by incident waves via the term $v\dot{r}$. In practice, a quadratic damping matrix is used to compensate for the difference between modelled and actual damping forces and moments while the coefficients in the matrix need to be calibrated case by case. Future work for improving numerical model of the drag forces, which able to model the drag forces with an acceptable accuracy in blind tests, is highly recommended.

The uncertainties in the simulated and measured low frequency surge and heave motions have negligible effects on the fore-aft bending moments in the five cross-sections in the hull. The low frequency fore-aft bending moments are dominated by the wind loads, and pitch motion

related fluctuations of gravity forces and hydrostatic pressure forces. The inertial load effect on the low frequency responses is limited except for responses with frequency components around the pitch natural frequency. Effect of the second and higher order wave excitation loads on the fore-aft bending moments is observed from the measurements and discussed. In general the effect is relatively limited in the analyzed operational conditions but can be critical in extreme conditions.

The differences in the simulated and measured wave-frequency rigid-body motions and fore-aft bending moments, for which the relative difference for standard deviation of the corresponding measurements and simulations is no more than 10%, are due to the difference between the simulated and actual first order and higher order wave excitation loads. Note that the second and higher order wave excitation loads are not included in the numerical models. The level of relative difference, which is due to uncertainties and noises in measurements, of standard deviations of the corresponding measurements and simulations could be around 2.48%. To further analyze the reason of the differences in the simulated and actual wave excitation loads on the hull, numerical modelling approach for full second order wave excitation loads should be developed, while the wave excitation loads on the hull, when the hull is fixed at its mean position in wind and waves, should be measured in future test programs. A preliminary comparison, which is scheduled to be published with a more comprehensive analysis in future, with respect to the simulated and measured responses in a 1-h extreme condition (the model test 2410) shows that the relative difference of the standard deviation and maximum value of the simulated and measured fore-aft bending moment are in the level of 7.3% and 55%, respectively. Note that more efforts are needed to quantify uncertainties in the measurements in the extreme condition, in particular for the 1-h maximum value.

The mean forces and moments from wind and waves result in a change in the configuration of the mean wetted body surface of the hull when compared to the configuration in calm water. This may result in a considerable change in the resultant sectional forces and moments even though the change in resultant of the hydro pressure forces on the whole wetted body surface could be very limited.

A summary of important load components on the simulated fore-aft bending moments in the five cross-sections is available in Table 11. Relative importance of load components on the fore-aft bending moments depends on wind and wave conditions, location of the cross-section in the hull, amplitudes and phase angles of rigid-body motions, and configuration of corresponding wetted body surface of the hull. The interface between the pontoons and central column is identified as the most critical part. Both the low frequency and wave frequency components of load effects could be important. From S1 to S3, value of standard deviation of the first order wave excitation load induced fore-aft bending moment increases. The effect of the fluctuation of the hydrostatic pressure on the wetted body surface of the hull and the fluctuation of the gravity forces are important to the fore-aft bending moments in the cross-sections in the tower and central column and in the cross-sections that are on the pontoons and close to the central column. The phase difference between the simulated surge and pitch motions can be close to 180 degrees in the frequency range from 0.4 rad/s to 0.6 rad/s and means a cancellation effect for the bending moments induced by the inertial loads which are associated to acceleration in surge and pitch. The inertial loads induced fore-aft bending moments in S3 are dominated by the inertial loads that are proportional to acceleration associated with heave motions.

In the analyzed environmental conditions, the convolutional terms have very limited effect on the simulations and could be removed from the numerical models to significantly reduce modelling complexity and computational cost for short-term analysis. The applicability of this simplification should be analyzed case by case since the importance of the convolution terms is related to configurations of the wetted body surface, and amplitudes and frequencies of the motions of the hull. This issue should be kept in mind in design of model tests in future.

Analysis presented in this paper substantiates that the simulated fore-aft bending moments of the model in wind and waves could be obtained by superimposing the corresponding simulations of the model subjected to its corresponding wind only condition, and wave only condition except that three constant forces and moments which are the corresponding averaged wind induced forces and moments are applied if the interaction effect between wind and wave loads and/or the interaction effect on the sectional forces and moments are limited. The simplification can significantly reduce computational cost but applicability of the simplification should be analyzed case by case.

Analysis and discussions given in this paper are based on available measurements. More systematical and step by step model tests for quantifying and minimizing uncertainties in measurements and identifying the first order and higher order wave excitation loads are welcome in future. While, the frequency dependent radiation and diffraction hydrodynamic loads are expected to be relatively more significant when volume in water and water plane area of the experimental model are relatively large and the experimental model is subjected to irregular waves for which major wave energy is in frequency range from 1 rad/s to 2 rad/s. Numerical and experimental analysis for the model in extreme conditions and fault conditions as described for example in [38–40] is scheduled as a future work.

The aerodynamic loads applied on the numerical models are prescriptive loads measured from the model tests. Analysis shows that the actual aerodynamic loads on the experimental model can be accurately measured. Consequently, the difference between the measurements and simulations only indicate differences in the hydro loads on the hull and the mass properties of the numerical and experimental models. If the deviation between the simulated and measured rigid-body motions is large, the prescriptive loads will fail to represent the right dependency of the aerodynamic loads with respect to the rigid-body motions. Fortunately, the agreement between the simulated and measured rigid-body motions is very good. This limitation can be avoided by developing a numerical model for the wind turbine of the experimental model to simulate the aerodynamic loads in the time-domain simulations based on numerical wind field and the simulated rigid-body motions. However, increase of uncertainties due to the differences between the numerical and actual wind fields, and the differences between performance of the numerical and experimental models of the wind turbine must be considered.

The time-domain approach used for developing numerical models analyzed in this paper is a generic approach that is applicable for static determinate and indeterminate structures. The approach could be used for long-term extreme load prediction and fatigue damage analysis while the understanding with respect to the wind and wave load effects on the sectional forces and moments could be helpful for structural optimization and control for the hull of floating wind turbines, for example, similar work with respect to the work presented in [42–45] could be done in future. According to the approach, a genetic structure can be discretized into several bodied for modeling hydro loads, which are based on coefficients that are obtained by solving the first order boundary value problem with the rigid-body assumption, in time-domain on each body while global flexibility of the structure can be modelled by using beam elements. Extension for accounting for hydroelastisity, e.g. [41], is scheduled as future work for development of the approach.

Acknowledgement

The authors acknowledge the financial support provided by the Research Council of Norway through the Centre for Ships and Ocean Structures; the Norwegian Research Centre for Offshore Wind Technology (NOWITECH), NTNU; and the Centre for Autonomous Marine Operations and Systems (AMOS), NTNU. Mr. Fredrik Brun from SINTEF Ocean (formerly MARINTEK) is acknowledged for providing Fig. 2.

Appendix A

Detailed observations of comparisons for identifying the dominant load components listed in Table 11 in Section 5.2 are analysed and described as follows:

- Components of $R_5^{s,S1}$ (realization of the fore-aft bending moment in base of side column 1) with oscillating frequencies in the low frequency-range are dominated by $\boldsymbol{L}^{e,gra,S1,A}$ and $\boldsymbol{L}^{e,sta,S1,A}$. Effects of the inertial loads and added mass loads with a constant coefficient matrix corresponding to infinite frequency of the corresponding Part A on $R_5^{s,S1}$ are negligible except for components of $R_5^{s,S1}$ with oscillating frequencies in frequency-range nearby natural frequencies of surge and pitch. Note that effects of second and higher order wave excitations are not included in the numerical models. Components of first-order wave excitations in the low frequency-range are negligible. Spectral densities of incident waves are given in Fig. 4. Components of $R_5^{s,S1}$ with oscillating frequencies in the wave-frequency-range are dominated by $\boldsymbol{L}^{e,waex,SX,A}$ and inertial loads and added mass loads with a constant coefficient matrix corresponding to infinite frequency of the corresponding Part A. See Fig. A1.
- Observations for components of $R_5^{s,S2}$ are similar to the observations for components of $R_5^{s,S1}$ as described in above except that effects of $\boldsymbol{L}^{e,gra,S2,A}$ and $\boldsymbol{L}^{e,sta,S2,A}$ on components of $R_5^{s,S2}$ with oscillating frequencies in the wave-frequency-range are not negligible. Note that $\boldsymbol{L}^{e,sta,S2,A}$ is related to rigid-body motions and configuration of the wetted body surface of the corresponding Part A. See Figs. A1 and A2.
- Observations for components of $R_5^{s,S3}$ are similar to the observations for components of $R_5^{s,S2}$ as described in above. See Figs. A2 and A3.
- The expression of equilibrium for $R_5^{s,S5}$ is given in Eq. (8). Inertial loads on the RNA and tower affect components of $R_5^{s,S5}$ with oscillating frequencies that are around pitch natural frequency, e.g. from 0.15 rad/s to 0.25 rad/s. Components of $R_5^{s,S5}$ with very small oscillating frequencies, e.g. below 0.15 rad/s, are dominated by wind loads on and gravity forces of the RNA and tower. The inertial loads of the RNA and tower strongly affect components of $R_5^{s,S5}$ with oscillating frequencies that are in the wave-frequency-range. While, effects of the wind loads on and gravity forces of the RNA and tower on these components are not negligible.
- Observations for components of $R_5^{s,S4}$ (realization of the fore-aft bending moment in base of the central column) with oscillating frequencies in the low frequency-range are similar to the observations for the corresponding components of $R_5^{s,S5}$. Observations for components of $R_5^{s,S4}$ with oscillating frequencies in the wave-frequency-range are similar to the observations for components of $R_5^{s,S2}$ except that effects thrust forces on the RNA and tower on the components of $R_5^{s,S4}$ with oscillating frequencies in the wave-frequency-range are not negligible. See Figs. A2–A5.

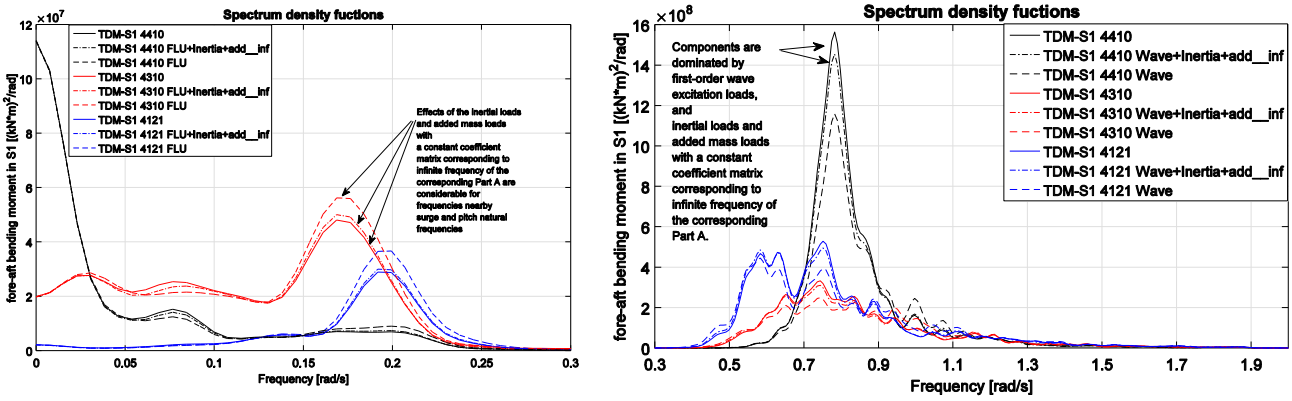

Fig. A1. Comparisons of spectral densities of simulated fore-aft bending moments in S1. Note that "Wave + Inertia + add_inf" corresponding to $\boldsymbol{R}^{waex,S1,A} + \boldsymbol{R}^{Inertia,S1,A} + \boldsymbol{R}^{add_inf,S1,A}$ while "Wave" corresponding to $\boldsymbol{R}^{waex,S1,A}$.

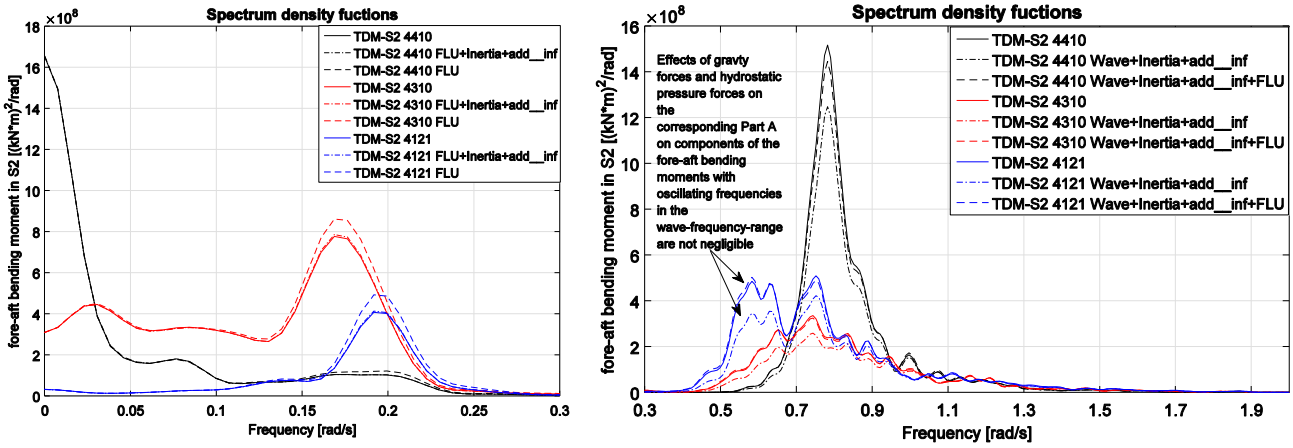

Fig. A2. Comparisons of spectral densities of simulated fore-aft bending moments in S2. Note that "Wave + Inertia + add_inf" corresponding to $\boldsymbol{R}^{waex,S2,A} + \boldsymbol{R}^{Inertia,S2,A} + \boldsymbol{R}^{add_inf,S2,A}$ while "FLU" corresponding to $\boldsymbol{R}^{flu,S2,A}$.

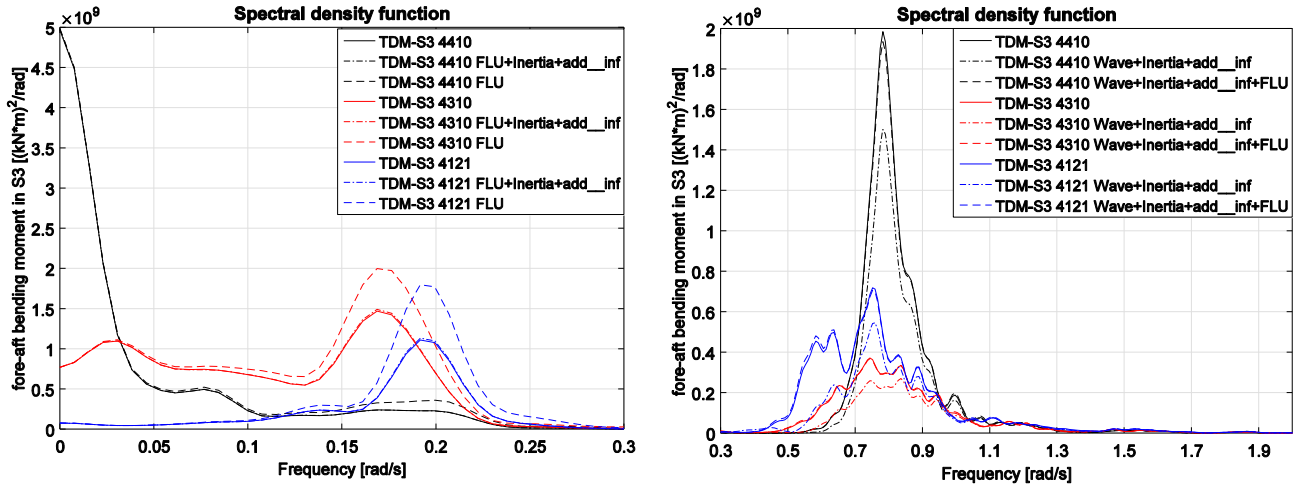

Fig. A3. Comparisons of spectral densities of simulated fore-aft bending moments in S3. Note that "Wave + Inertia + add_inf" corresponding to $\boldsymbol{R}^{waex,S3,A}$ + $\boldsymbol{R}^{Inertia,S3,A}$ + $\boldsymbol{R}^{add_inf,S3,A}$ while "FLU" corresponding to $\boldsymbol{R}^{flu,S3,A}$.

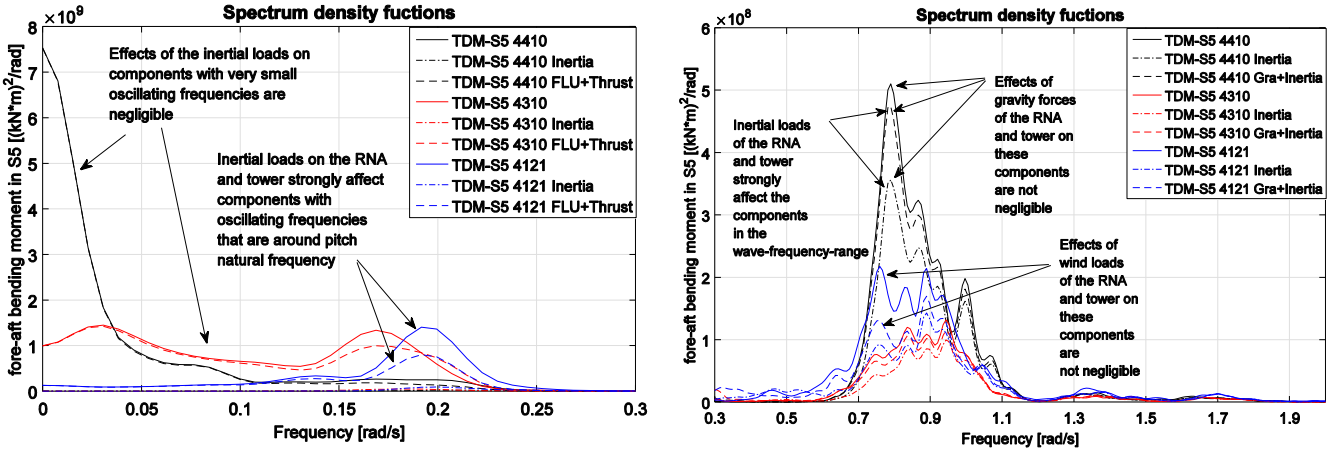

Fig. A4. Comparisons of spectral densities of simulated fore-aft bending moments in S5. Note that "Inertia" corresponding to $\boldsymbol{R}^{Inertia,S5,B}$ while "Gra" corresponding to $\boldsymbol{R}^{flu,S5,B}$.

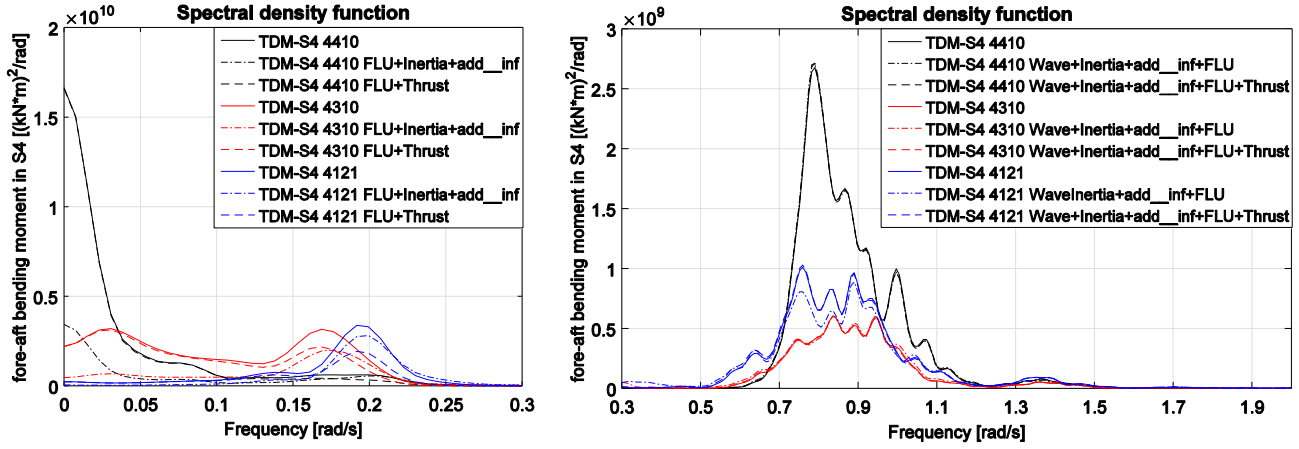

Fig. A5. Comparisons of spectral densities of simulated fore-aft bending moments in S4. Note that "Wave + Inertia + add_inf + FLU" corresponding to $\boldsymbol{R}^{waex,S4,B}$ + $\boldsymbol{R}^{Inertia,S4,B}$ + $\boldsymbol{R}^{add_inf,S4,B}$ + $\boldsymbol{R}^{flu,S4,B}$ while "Thrust" corresponding to $\boldsymbol{R}^{Thrust,S4,B}$.

Appendix B

Spectral densities of rigid-body motions and fore-aft bending moments in the five cross-sections given by numerical models with and without the convolution terms in the expressions of radiation loads on each part of the hull are compared. Numerical model without the convolution term means that 1) the potential damping forces are not modelled, and 2) the frequency dependent added mass coefficients are replaced by added mass coefficients that corresponding to the high-frequency limit (see Figs. B1-B4).

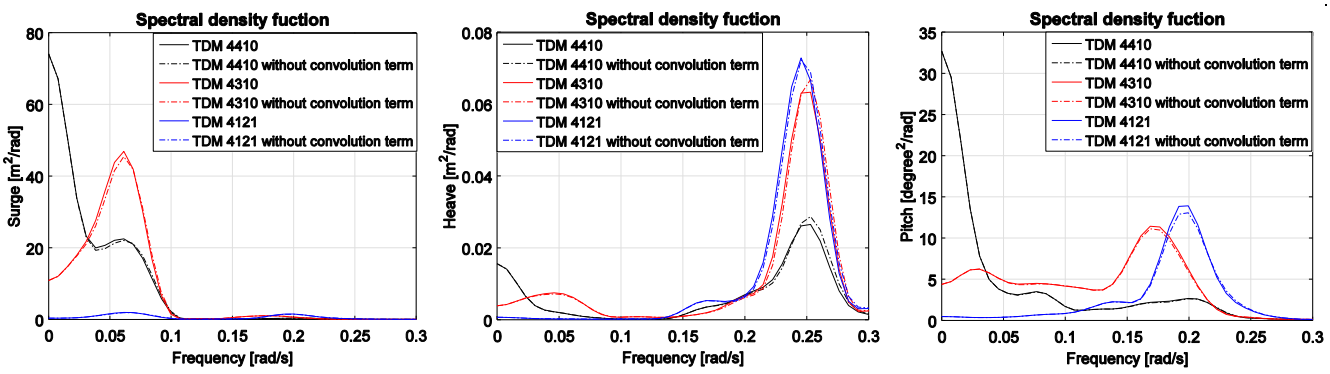

Fig. B1. Comparisons of spectral densities of simulated surge, heave and pitch motions with and without the convolution terms in frequency range from 0 rad/s to 0.3 rad/s.

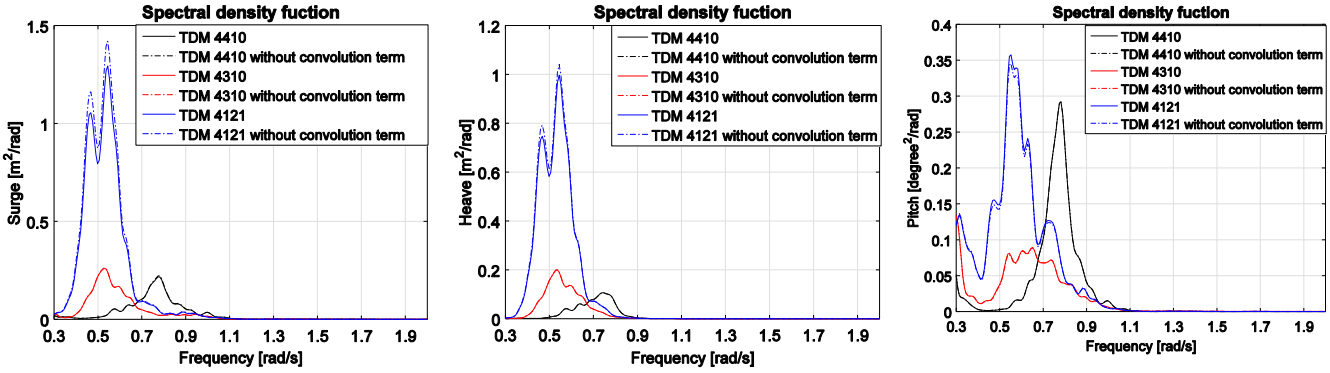

Fig. B2. Comparisons of spectral densities of simulated surge, heave and pitch motions with and without the convolution terms in frequency range from 0.3 rad/s to 2 rad/s.

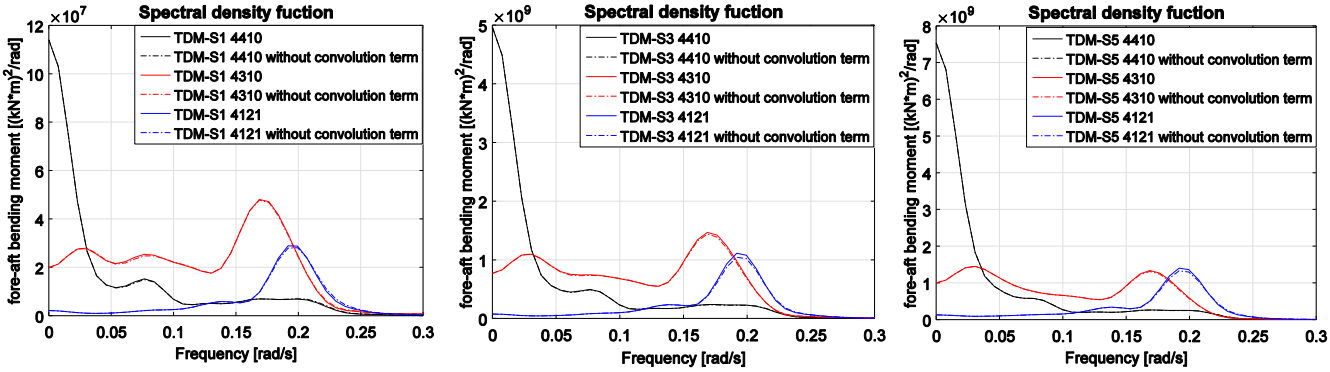

Fig. B3. Comparisons of spectral densities of simulated fore-aft bending moment with and without the convolution terms in frequency range from 0 rad/s to 0.3 rad/s.

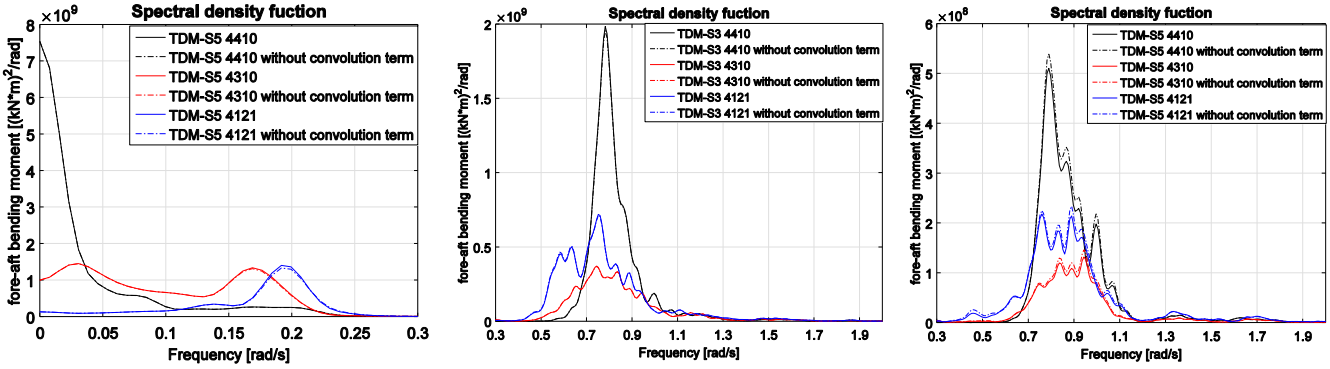

Fig. B4. Comparisons of spectral densities of simulated fore-aft bending moment with and without the convolution terms in frequency range from 0.3 rad/s to 2 rad/s.

References

[1] IEC, Wind turbines – Part 1: Design requirements, IEC-61400-1, International Electrotechnical Commission; 2005.

[2] IEC, Wind turbines: Part 3: Design requirements for offshore wind turbines, IEC-61400-3, International Electrotechnical Commission; 2009.

[3] DNV, Offshore standard – Design of Offshore Wind Turbine Structures, DNV-OS-J101, Det Norske Veritas; 2013.

[4] GL, Guideline for the certification of Wind Turbines. Germanischer Lloyd, Hamburg, Germany; 2010.

[5] DNV, Offshore standard – Design of Floating Wind turbine Structures, DNV-OS-J103, Det Norske Veritas; 2013.

[6] Cordle A, Jonkman J. State of the art in floating wind turbine design tools. In: Proceedings of the 21st international offshore and polar engineering conference, Maui, Hawaii, USA. vol. 1; 2011. p. 367–74.

[7] Matha D, Schlipf M, Cordle A, Pereira R, Jonkman J. Challenges in simulation of aerodynamics, hydrodynamics, and mooring-line dynamics of floating offshore wind turbines. In: Proceedings of the 21st international offshore and polar engineering conference, Maui, Hawaii, USA, vol. 1; 2011. p. 421–8.

[8] Robertson A, Jonkman J, Qvist J, Chen X, Armendariz JA, Soares CG, et al. Offshore code comparison collaboration, continued: phase II results of a floating semi-submersible wind system", In: Proceedings of the 33rd international conference on ocean, offshore and arctic engineering, no. OMAE2014-24040, San Francisco, USA; 2014.

[9] Luan C, Gao Z, Moan T. Development and verification of a time-domain approach for determining forces and moments in structural components of floaters with an application to floating wind turbines. Mar Struct 2017;5:87–109.

[10] Kvittem MI, Bachynski EE, Moan T. Effects of hydrodynamic modelling in fully coupled simulations of a semi-submersible wind turbine. Energy Proc 2012;24:351–62. https://doi.org/10.1016/j.egypro.2012.06.118.

[11] Luan C, Chabaud V, Bachynski E, Gao Z, Moan T. Experimental validation of a time-domain approach for determining sectional loads in a floating wind turbine hull subjected to moderate waves, accepted for publication at Energy Procedia.

[12] Goupee AJ, Koo BJ, Lambrakos K, Kimball RW. Model tests for three floating wind turbine concepts. In: Proceedings of the 2012 Offshore Technology Conference, Houston, Texas, USA, 30 April 2012–3 May 2012.

[13] Goupee AJ, Koo B, Kimball RW, Lambrakos KF, Dagher HJ. Experimental comparison of three floating wind turbine concepts. In: Proceedings of the 31st ASME international conference on offshore mechanics and arctic engineering, Rio de Janeiro, Brazil; 1–6 July 2012.

[14] B. Koo, A. J. Goupee, K. Lambrakos, and R. W. Kimball, "Model tests for a floating wind turbine on three different floaters," in Proceedings of the 31st ASME International Conference on Offshore Mechanics and Arctic Engineering, Rio de Janeiro, Brazil, 1–6 July 2012.

[15] Roddier D, Cermelli C, Aubault A, Weinstein A. WindFloat: a floating foundation for offshore wind turbines. J Renew Sustain Energy 2010;2. https://doi.org/10.1063/1.3435339.

[16] Wan L, Gao Z, Moan T. Experimental and numerical study of hydrodynamic responses of a combined wind and wave energy converter concept in survival modes. Coast Eng 2015;104:151–69.

[17] Kimball R, Goupee AJ, Fowler MJ, de Ridder E-J, Helder J. Wind/wave basin verification of a performance-matched scale-model wind turbine on a floating offshore wind turbine platform. In: Proceedings of the ASME 2014 33rd International Conference on Ocean, Offshore and Arctic Engineering, no. OMAE2014-24166; 2014.

[18] Fowler MJ, Kimball RW, Thomas DA, Goupee AJ. Design and testing of scale model wind turbines for use in wind/wave basin model tests of floating offshore wind turbines. In: 32nd International Conference on Ocean, Offshore and Arctic Engineering, no. OMAE2013-10122; 2013.

[19] Bottasso CL, Campagnolo F, Pectrovic V. Wind tunnel testing of scaled wind turbine models: Beyond aerodynamics. J Wind Eng Ind Aerodyn 2014;127:11–28.

[20] Fernandes G, Make M, Gueydon S, Vaz G. Sensitivity to aerodynamic forces for the accurate modelling of floating offshore wind turbines. In: RENEW2014, G. Soares, ed., no. ISBN: 978-1-138-02871-5; 2014.

[21] Helder J, Pietersma M. UMAINE-DEEPCWIND/OC4 SEMIFLOATING WIND TURBINE, 27005-1-OB. Wageningen, NL:MARIN; 2013.

[22] Sauder T, Chabaud V, Thys M, Bachynski EE, Sæther LO. Real-time hybrid model testing of a braceless semi-submersible wind turbine: Part I: The hybrid approach. In: 35th International conference on ocean, offshore and arctic engineering, no. OMAE2016-54435; 2016.

[23] Hall M, Goupee A, Jonkman J. Development of performance specifications for hybrid modeling of floating wind turbines in wave basin tests. J Ocean Eng Mar Energy 2017.

[24] Laino D, Hansen C. User's guide to the wind turbine aerodynamics computer software Aerodyn, Windward Engineering, Prepared for the National Renewable Energy Laboratory under Subcontract No. TCX-9-29209-01; 2002.

[25] Bachynski EE, Thys M, Chabaud V, Sauder T. Realtime hybrid model testing of a Braceless semi-submersible wind turbine. Part II: Experimental results. In: 35th International conference on ocean, offshore and arctic engineering, no OMAE2016-54437; 2016.

[26] Chabaud V. Real-Time Hybrid Model Testing of Floating Wind Turbines. Ph.d thesis, ISBN 978-82-326-2083-8., NTNU, Norway; 2016.

[27] Wendt F, Robertson A, Jonkman J. FAST model calibration and validation of the OC5-DeepCwind floating offshore wind system against wave tank test data. In: The 27th International Ocean and Polar Engineering Conference, San Francisco, California, U.S.A.; 2017.

[28] Ormberg H, Baarholm R, Stansberg CT. Time-domain coupled analysis of deepwater TLP, and verification against model tests. In: Proc. 13th ISOPE Conf., Honolulu, Hawaii, USA; 2003.

[29] MARINTEK. SIMO User's Manual; 2011.

[30] MARINTEK. RIFLEX User's Manual; 2013.

[31] DNV, Recommended Practice – Environmental Conditions and Environmental Loads, DNV-RP-C205, Det Norske Veritas; 2010.

[32] Berthelsen PA, Bachynski EE, Karimirad M, Thys M. Real-time hybrid model testing of a braceless semi-submersible wind turbine. Part III: Calibration of a numerical model. In: 35th International Conference on Ocean, Offshore and Arctic Engineering, no. OMAE2016-54640; 2016.

[33] Luan C, Gao Z, Moan T. Design and analysis of a braceless steel 5-mw semi-submersible wind turbine. In: Proceedings of the 35th International Conference on Ocean, Offshore and Arctic Engineering, OMAE2016-54848, Busan, Korea; June 19–24 2016.

[34] Naess A, Moan T. Stochastic dynamics of marine structures. UK: Cambridge University Press; 2013.

[35] Bendat JS, Piersol AG. Random data: Analysis and measurement procedures ISBN: 978-0-470-24877-5 4th ed. John Wiley & Sons, Inc.; 2010. p. 180.

[36] Sclavounos P, Zhang Y, Ma Y, Larson D. Offshore wind turbine nonlinear wave loads and their statistics. In: 36th International Conference on Ocean, Offshore and Arctic Engineering, no. OMAE2017-61184; 2017.

[37] Faltinsen OM. Sea loads on ships and offshore structures. UK: Cambridge University Press; 1990.

[38] Jiang Z, Moan T, Gao Z. A comparative study of shutdown procedures on the dynamic responses of wind turbines. J Offshore Mech Arct Eng 2015;137(1):011904.

[39] Jiang Z, Karimirad M, Moan T. Response analysis of parked spar-type wind turbine considering blade-pitch mechanism fault. Int J Offshore Polar Eng 2013;23(02).

[40] Jiang Z, Karimirad M, Moan T. Dynamic response analysis of wind turbines under blade pitch system fault, grid loss, and shutdown events. Wind Energy 2014;17(9):1385–409.

[41] Watanabe E, Utsunomiya T, Wang C, Hang L. Benchmark hydroelastic responses of a circular VLFS under wave action. Eng Struct 2006;28:423–30.

[42] Colwell S, Basu B. Tuned liquid column damper in offshore wind turbines for structural control. Eng Struct 2009;31:358–68.

[43] Agarwal P, Manuel L. Simulation of offshore wind turbine response for long-term extreme load prediction. Eng Struct 2009;31:2236–46.

[44] Dong W, Moan T, Gao Z. Long-term fatigue analysis of multi-planar tubular joints for jacket-type offshore wind turbine in time domain. Eng Struct 2011;33:2002–14.

[45] Si Y, Karimi H, Gao H. Modelling and optimization of a passive structural control design for a spar-type floating wind turbine. Eng Struct 2014;69:168–82.

[46] Le Méhauté B. An introduction to hydrodynamics and water waves. Technical Report ERL 118-POL-3-2. U.S. Department of Commerce, Washington DC; 1969.